

# The ATLAS<sup>3D</sup> project – I. A volume-limited sample of 260 nearby early-type galaxies: science goals and selection criteria

Michele Cappellari,<sup>1\*</sup> Eric Emsellem,<sup>2,3</sup> Davor Krajnović,<sup>2</sup> Richard M. McDermid,<sup>4</sup> Nicholas Scott,<sup>1</sup> G. A. Verdoes Kleijn,<sup>5</sup> Lisa M. Young,<sup>6</sup> Katherine Alatalo,<sup>7</sup> R. Bacon,<sup>3</sup> Leo Blitz,<sup>7</sup> Maxime Bois,<sup>2,3</sup> Frédéric Bournaud,<sup>8</sup> M. Bureau,<sup>1</sup> Roger L. Davies,<sup>1</sup> Timothy A. Davis,<sup>1</sup> P. T. de Zeeuw,<sup>2,9</sup> Pierre-Alain Duc,<sup>10</sup> Sadeh Khochfar,<sup>11</sup> Harald Kuntschner,<sup>12</sup> Pierre-Yves Lablanche,<sup>3</sup> Raffaella Morganti,<sup>5,13</sup> Thorsten Naab,<sup>14</sup> Tom Oosterloo,<sup>5,13</sup> Marc Sarzi,<sup>15</sup> Paolo Serra<sup>13</sup> and Anne-Marie Weijmans<sup>16†</sup>

<sup>1</sup>Sub-department of Astrophysics, Department of Physics, University of Oxford, Denys Wilkinson Building, Keble Road, Oxford OX1 3RH

<sup>2</sup>European Southern Observatory, Karl-Schwarzschild-Str. 2, 85748 Garching, Germany

<sup>3</sup>Université Lyon 1, Observatoire de Lyon, Centre de Recherche Astrophysique de Lyon and Ecole Normale Supérieure de Lyon, 9 avenue Charles André, F-69230 Saint-Genis Laval, France

<sup>4</sup>Gemini Observatory, Northern Operations Centre, 670 N. A'ohoku Place, Hilo, HI 96720, USA

<sup>5</sup>Kapteyn Astronomical Institute, University of Groningen, Postbus 800, 9700 AV Groningen, the Netherlands

<sup>6</sup>Physics Department, New Mexico Institute of Mining and Technology, Socorro, NM 87801, USA

<sup>7</sup>Department of Astronomy, Campbell Hall, University of California, Berkeley, CA 94720, USA

<sup>8</sup>Laboratoire AIM Paris-Saclay, CEA/IRFU/SAP CNRS Université Paris Diderot, 91191 Gif-sur-Yvette Cedex, France

<sup>9</sup>Sterrewacht Leiden, Leiden University, Postbus 9513, 2300 RA Leiden, the Netherlands

<sup>10</sup>Laboratoire AIM, CEA/DSM-CNRS-Université Paris Diderot, Dapnia/Service d'Astrophysique, CEA-Saclay, 91191 Gif-sur-Yvette Cedex, France

<sup>11</sup>Max-Planck Institut für extraterrestrische Physik, PO Box 1312, D-85478 Garching, Germany

<sup>12</sup>Space Telescope European Coordinating Facility, European Southern Observatory, Karl-Schwarzschild-Str. 2, 85748 Garching, Germany

<sup>13</sup>Netherlands Institute for Radio Astronomy (ASTRON), Postbus 2, 7990 AA Dwingeloo, the Netherlands

<sup>14</sup>Max-Planck Institut für Astrophysik, Karl-Schwarzschild-Str. 1, 85741 Garching, Germany

<sup>15</sup>Centre for Astrophysics Research, University of Hertfordshire, Hatfield, Herts AL1 9AB

<sup>16</sup>Dunlap Institute for Astronomy & Astrophysics, University of Toronto, 50 St. George Street, Toronto, ON M5S 3H4, Canada

Accepted 2010 December 8. Received 2010 December 6; in original form 2010 November 2

## ABSTRACT

The ATLAS<sup>3D</sup> project is a multiwavelength survey combined with a theoretical modelling effort. The observations span from the radio to the millimetre and optical, and provide multi-colour imaging, two-dimensional kinematics of the atomic (H I), molecular (CO) and ionized gas (H $\beta$ , [O III] and [N I]), together with the kinematics and population of the stars (H $\beta$ , Fe5015 and Mg *b*), for a carefully selected, volume-limited ( $1.16 \times 10^5$  Mpc<sup>3</sup>) sample of 260 early-type (elliptical E and lenticular S0) galaxies (ETGs). The models include semi-analytic, *N*-body binary mergers and cosmological simulations of galaxy formation. Here we present the science goals for the project and introduce the galaxy sample and the selection criteria. The sample consists of nearby ( $D < 42$  Mpc,  $|\delta - 29^\circ| < 35^\circ$ ,  $|b| > 15^\circ$ ) morphologically selected ETGs extracted from a *parent* sample of 871 galaxies (8 per cent E, 22 per cent S0 and 70 per cent spirals) brighter than  $M_K < -21.5$  mag (stellar mass  $M_\star \gtrsim 6 \times 10^9 M_\odot$ ). We analyse possible selection biases and we conclude that the parent sample is essentially complete and statistically representative of the nearby galaxy population. We present the size–luminosity relation for the spirals and ETGs and show that the ETGs in the ATLAS<sup>3D</sup> sample define a

\*E-mail: cappellari@astro.ox.ac.uk

†Dunlap fellow.

tight red sequence in a colour–magnitude diagram, with few objects in the transition from the blue cloud. We describe the strategy of the SAURON integral field observations and the extraction of the stellar kinematics with the pPXF method. We find typical  $1\sigma$  errors of  $\Delta V \approx 6 \text{ km s}^{-1}$ ,  $\Delta\sigma \approx 7 \text{ km s}^{-1}$ ,  $\Delta h_3 \approx \Delta h_4 \approx 0.03$  in the mean velocity, the velocity dispersion and Gauss–Hermite (GH) moments for galaxies with effective dispersion  $\sigma_e \gtrsim 120 \text{ km s}^{-1}$ . For galaxies with lower  $\sigma_e$  ( $\approx 40$  per cent of the sample) the GH moments are gradually penalized by pPXF towards zero to suppress the noise produced by the spectral undersampling and only  $V$  and  $\sigma$  can be measured. We give an overview of the characteristics of the other main data sets already available for our sample and of the ongoing modelling projects.

**Key words:** galaxies: distances and redshifts – galaxies: elliptical and lenticular, cD – galaxies: evolution – galaxies: formation – galaxies: kinematics and dynamics – galaxies: structure.

## 1 INTRODUCTION

### 1.1 Scientific background

Observations of high-redshift galaxies and the cosmic microwave background (Spergel et al. 2007) have revealed the Universe to be dominated by dark matter and dark energy (Riess et al. 1998; Perlmutter et al. 1999), providing a working paradigm for the formation of structure (e.g. Springel et al. 2005b). However, the mechanisms that form the luminous content of the dark matter potential (i.e. the stars and galaxies that we observe) remain the key unknowns of modern extragalactic astronomy. These processes are driven by the hydrodynamics and chemistry of the gas, combined with complex radiative feedback processes. High-redshift observations alone are not sufficient to constrain these processes, lacking spectral information and spatial resolution (Faber et al. 2007). It is therefore necessary to complement these studies with detailed analysis of nearby objects, tracing the *fossil record* of the formation process. Early-type (elliptical E and lenticular S0) galaxies (ETGs) are especially useful as they are old, have smaller levels of star formation and limited amount of dust, which simplifies the interpretation of the observations. Significant progress has been made in this direction in the past few decades, building on the classic observational works that still capture much of our understanding of the structure of local ETGs (e.g. Hubble 1936; Faber & Jackson 1976; Davies et al. 1983; Djorgovski & Davis 1987; Dressler et al. 1987; Bender, Burstein & Faber 1992; Kormendy & Richstone 1995).

A major step forward was brought by the era of large galaxy surveys. Thanks to the unprecedented sample size, one of the most important contributions of the Sloan Digital Sky Survey (SDSS; York et al. 2000) was to firmly establish a statistically significant bimodality in the colour distribution of local galaxies, such that they can be clearly separated in a so-called ‘blue cloud’, generally consisting of star-forming spiral galaxies, and a ‘red sequence’, mostly of non-star-forming ETGs (Strateva et al. 2001; Baldry et al. 2004). Accurately quantifying this bimodality, and the realization that it can be traced back in time to higher redshift (Bell et al. 2004; Faber et al. 2007), allowed a dramatic improvement in the detailed testing of galaxy formation scenarios.

The bimodality can only be explained with the existence of a mechanism, which suppresses episodes of intense star formation by evacuating gas from the system, resulting in a rapid transition of galaxies from the blue cloud to the red sequence (Springel, Di Matteo & Hernquist 2005a; Faber et al. 2007). Many simulation groups have reproduced the bimodality qualitatively, though with

rather different assumptions for the star formation and feedback processes (Granato et al. 2004; Di Matteo, Springel & Hernquist 2005; Bower et al. 2006; Cattaneo et al. 2006; Croton et al. 2006). A generic feature of these models is that red-sequence galaxies form by dissipational ‘wet mergers’ of gas-rich blue-cloud galaxies, followed by quenching of the resulting intense star formation by rapid ejection of the gas, caused by the feedback from a central supermassive black hole, supernovae winds, by shock heating of the gas in the most massive haloes (Kereš et al. 2005; Dekel & Birnboim 2006) or gravitational gas heating (Naab et al. 2007; Khochfar & Ostriker 2008; Johansson, Naab & Ostriker 2009). The merging of the most massive blue galaxies, however, is not sufficient to explain the population of most massive red-sequence galaxies. Dissipationless ‘dry mergers’ of gas-poor, red-sequence galaxies is therefore also required, evolving galaxies *along* the red sequence as they increase in mass (Khochfar & Burkert 2003; Naab, Khochfar & Burkert 2006b; Hopkins et al. 2009; Khochfar & Silk 2009; Oser et al. 2010).

Both wet and dry major mergers generally produce red, bulge-dominated galaxies when feedback is included in the models. The kinematic structure of the remnants is however very different. In a major (1:1) merger between blue gas-rich galaxies, the gas tends to form a disc, so that the end result of the merger, after the gas has been removed from the system by ejection, heating or conversion to stars, will be a red stellar system dominated by rotation (Cox et al. 2006; Naab et al. 2006a; Robertson et al. 2006; Jesseit et al. 2009). In major mergers between red gas-poor galaxies, dissipationless processes dominate, resulting in a red galaxy with little or no net rotation (Barnes 1992; Hernquist 1992; Naab, Burkert & Hernquist 1999; Naab & Burkert 2003; Cox et al. 2006). Unlike major mergers, minor mergers (1:3 or less) retain more closely the structure of the progenitor, to an extent that depends on the amount of mass and gas accreted, so that the remnant of a spiral galaxy will always display significant rotation (Naab et al. 2006a; Robertson et al. 2006; Bournaud, Jog & Combes 2007; Jesseit et al. 2009). These simulations demonstrate that if galaxies assemble by mergers, the existence of the red/blue galaxies dichotomy therefore also suggests the existence of a *kinematical* differentiation *within* the red sequence between fast and slow rotating galaxies.

Various classic observational indicators of a ETGs dichotomy have been proposed in the past two decades. ETGs have been found to exhibit trends as a function of luminosity in terms of (i) their distribution on the  $(V/\sigma, \epsilon)$  diagram, which relates the ratio of ordered  $V$  and random  $\sigma$  stellar motion to the galaxy ellipticity  $\epsilon$  (e.g. Illingworth 1977; Binney 1978; Davies et al. 1983), (ii) their

isophote shape (discy or boxy) (Bender et al. 1989; Kormendy & Bender 1996), (iii) the inner slope of their photometric profiles: cored/cuspy (Ferrarese et al. 1994; Lauer et al. 1995; Faber et al. 1997) or excess/deficit of core light (Graham 2004; Ferrarese et al. 2006; Kormendy et al. 2009). However, none of these signatures has been able to give clear evidence for a distinction between the two classes of red-sequence galaxies, primarily because they are all essentially secondary indicators of the galaxies’ internal kinematic structure.

By the application of integral field spectroscopy to a representative sample of nearby ETGs, the SAURON survey (de Zeeuw et al. 2002) has revealed the full richness of the kinematics of these objects (Emsellem et al. 2004; McDermid et al. 2006; Krajnović et al. 2008). From the two-dimensional nature of this unique data set, two distinct morphologies of stellar rotation fields are clearly evident, corresponding to the above described fast- and slow rotators. In two companion papers of that survey a global quantitative measure of this morphology was defined, termed  $\lambda_R$ , that can be used to kinematically classify these galaxies in a way that is more robust than the  $(V/\sigma, \epsilon)$  diagram and is nearly insensitive to projection effects (Emsellem et al. 2007; Cappellari et al. 2007).  $\lambda_R$  relates directly to their formation, and is precisely reproducible in current cosmological simulations (Jesseit et al. 2009; Bois et al. 2010). This is the basic new finding we plan to exploit in the present project to improve our understanding of the structure and formation of ETGs. Additional results of the SAURON survey on ETGs include the robustness and empirical ‘calibration’ of the simple virial mass estimator to measure mass in the central parts of ETGs and a determination of their dark matter fraction (Cappellari et al. 2006). The survey found a high incidence of ionized gas in ETGs (Sarzi et al. 2006) and explained their ionization mechanism as mainly due to the evolved stellar population (Sarzi et al. 2010). It was shown that the stellar population gradients correlate well with the escape velocity, both locally within galaxies and globally among different ETGs (Scott et al. 2009). Star formation in ETGs only happens in fast rotators and follows two distinct modes: in discs or widespread (Shapiro et al. 2010), where the latter cases are in low-mass systems (Jeong et al. 2009; Kuntschner et al. 2010). Discs in fast rotators have enhanced metallicity, while kinematically distinct cores in slow rotators show no stellar population signatures (Kuntschner et al. 2006, 2010).

## 1.2 Goals of the project

Because of the exploratory character of the SAURON survey (de Zeeuw et al. 2002), the ETGs were selected to sample, with a relatively small number of objects, a wide range of masses, shapes and morphologies. This was done by selecting galaxies brighter than a total magnitude  $M_B < -18$  mag equally subdivided into 24 E and 24 S0. Within each E/S0 subclass the selected objects sample uniformly a grid in the  $(M_B, \epsilon)$  plane. Although that approach was crucial in bringing the fast/slow rotator dichotomy to light and in most of the findings mentioned in the previous section, the selection criteria impose complex biases and do not allow for a quantitative statistical comparisons of galaxy properties with simulations, which is a main goal of the ATLAS<sup>3D</sup> project. Moreover, with only 48 galaxies, the statistical uncertainties are large.

The power of the kinematic classification based on  $\lambda_R$  is to be able to study differences in the formation process along the red-sequence galaxy population. The  $\lambda_R$  parameter describes in a compact way the present status of the galaxies, however, it is essential to obtain information on the formation history and the detailed dynamical structure as well. The stellar population contains a record of the

more distant history (a few Gyr). Recent gas accretion is recorded in the cold atomic gas components, generally detected on galaxy scales with radio observations of H I, while the ongoing accretion and star formation activity is traced by cold molecular gas (e.g. CO), often detected in regular discs in the central regions. For comparison with theoretical predictions one needs to observe all these quantities for a statistically significant, volume-limited sample of galaxies complete to some useful lower limit in mass. With these ideas in mind we carefully selected the ATLAS<sup>3D</sup> sample of ETGs and we systematically observed all the above quantities. The ATLAS<sup>3D</sup> data set now provides a complete inventory of the baryon budget and a detailed two-dimensional description of stellar and gaseous kinematics, together with resolved stellar population within the main body of a complete and statistically significant sample of ETGs. Our goal is to use this data set to perform archaeological cosmology by specifically answering the following questions.

(i) How do slow rotators form? What are the physical processes that determine their kinematic and photometric features? What is the role of major and minor mergers in their formation history? This will be reflected in the kinematics, gas content and stellar population.

(ii) Why are most ETGs fast rotators? There seems to be a dominant formation mechanism that delivers galaxies with quite homogeneous rotation properties. Can this be merging? Can significant major merging be excluded?

(iii) How is star formation in ETGs quenched? Is it different for fast- and slow-rotators ETGs? How does it depend on environment? Can we infer the quenching mechanism from the amount and distribution of the leftover gas, the presence of active galactic nuclei (AGN) or metallicity gradients? The distribution of stellar population and gas properties constitutes a stringent test for future galaxy formation models.

(iv) Most past studies have focused on single stellar population models of ETGs, but cosmological models predict more complex histories. Can we infer the star formation history in ETGs for detailed comparison with simulations?

(v) How do counter rotating cores in massive and old ETGs form and survive to the present time? Are these relics of the very early Universe?

(vi) Can we link the present day properties of ETGs to results from existing and upcoming surveys at higher redshift with respect to e.g. masses, sizes, stellar populations, gas fractions, star formation? Our study will constitute a  $z = 0$  redshift benchmark to trace the time evolution of galaxies.

The ATLAS<sup>3D</sup> sample includes all nearby ETGs observable from the northern Earth hemisphere, and for this reason we hope its homogeneous data set will ultimately constitute a legacy for future studies. We trust that our and other groups will exploit our data and sample well beyond what we had originally envisioned. Our first steps in the directions outlined above are presented in the following papers, while the other aspects will be presented in subsequent papers of this series:

(i) Krajnović et al. (2011, hereafter Paper II), which describes the morphology of the kinematics and the kinematical misalignment in ETGs;

(ii) Emsellem et al. (2011, hereafter Paper III), which presents a census of the stellar angular momentum in the central region of ETGs;

(iii) Young et al. (2011, hereafter Paper IV), which quantifies the distribution of molecular gas content in ETGs;

(iv) Davis et al. (2011, hereafter Paper V), which studies the Tully & Fisher (1977) relation from the width of the molecular lines in ETGs;

(v) Bois et al. (2011, hereafter Paper VI), which studies the formation of the fast- and slow-rotator galaxies via numerical simulations of binary mergers;

(vi) Cappellari et al. (2011, hereafter Paper VII), which revisits the morphology of nearby galaxies and presents the *kinematic morphology–density* relation;

(vii) Khochfar et al. (2011, hereafter Paper VIII), which studies the formation of ETGs using semi-analytic modelling.

Here in Section 2 we discuss the selection criteria for the *parent* sample of galaxies, from which the ATLAS<sup>3D</sup> sample of ETGs was extracted (Section 3). In Section 4 we present the SAURON observing strategy for the survey, the integral field data and the kinematic extraction, while other additional data sets and simulations from our project are listed in Section 5. We give a summary in Section 6. In the paper we assume  $H_0 = 72 \text{ km s}^{-1} \text{ Mpc}^{-1}$ .

## 2 THE PARENT SAMPLE

### 2.1 Selection criteria

Our final ATLAS<sup>3D</sup> sample will focus on ETGs only, however, before any morphological classification, we want to select all galaxies in the nearby volume above a certain total stellar mass. As we did not have dynamical information for all galaxies in the local volume at the beginning of our survey, the best proxy for mass available was the near-infrared ( $\sim 2.2 \mu\text{m}$ )  $K_s$ -band luminosity provided by the Two Micron All Sky Survey (2MASS; Skrutskie et al. 2006), which is unique for its full sky completeness and excellent photometric homogeneity. The  $K_s$  band is 5–10 times less sensitive to dust absorption than optical wavelengths and therefore can be used to select both dust-rich spirals and dust-poor ETGs to a similar mass level. Moreover the mass-to-light ratio of the stars in the near-infrared varies only about a factor  $\approx 2$ , which is about three times less than at optical wavelengths (Bell & de Jong 2001; Maraston 2005), thus providing a better approximation to the stellar mass than an optical selection.

To derive luminosities from the observed apparent magnitudes we need distances. Numerous accurate determinations have been accumulated in the literature in the past few years. However, we will resort to redshift distances when a more accurate distance is not available. In addition we enforce obvious observability criteria. This leads to the following selection steps.

(i) Choose a representative local volume with radius  $D = 42 \text{ Mpc}$ . It approximates the redshift selection  $cz < 3000 \text{ km s}^{-1}$  of the SAURON survey, for an adopted  $H_0 = 72 \text{ km s}^{-1} \text{ Mpc}^{-1}$  (Dunkley et al. 2009). It makes sure that key spectral features, such as H $\beta$ , [O III] and Mg  $b$ , fall within the SAURON wavelength range and allows for a significant overlap with previous observations.

(ii) Specify the observability criterion from the William Herschel Telescope (WHT) on La Palma  $|\delta - 29^\circ| < 35^\circ$ , where  $\delta$  is the sky declination.

(iii) Exclude the dusty region near the Galaxy equatorial plane  $|b| < 15^\circ$ , with  $b$  the galactic latitude.

(iv) Select all galaxies from the 2MASS extended source catalog (XSC; Jarrett et al. 2000) with apparent total magnitude  $K_T < 11.6 \text{ mag}$  (defined by the XSC parameter `k_m_ext`) and satisfying the observability criteria (ii) and (iii). Given the near completeness of the XSC down to  $K_T \approx 13.5 \text{ mag}$ , this selection is essentially

**Table 1.** Selection criteria for the galaxies in the ATLAS<sup>3D</sup> parent sample.

Distance:	$D < 42 \text{ Mpc}$
Galaxies total mag:	$M_K < -21.5 \text{ mag}$
Observability:	$ \delta - 29^\circ  < 35^\circ$
Galaxy zone of avoidance:	$ b  > 15^\circ$

**Table 2.** Main characteristics of the ATLAS<sup>3D</sup> parent sample.

Survey volume:	$\text{Vol} = 1.16 \times 10^5 \text{ Mpc}^3$
Galaxy $K$ -band luminosity:	$L > 8.2 \times 10^9 L_{\odot,K}$
Galaxy stellar mass:	$M_* \gtrsim 6 \times 10^9 M_{\odot}$
Galaxy $B$ -band total mag:	$M_B \lesssim -18.0 \text{ mag}$
Galaxy SDSS $r$ -band total mag:	$M_r \lesssim -18.9 \text{ mag}$
Total number of galaxies:	$N_{\text{gal}} = 871$
Spiral and irregular galaxies:	$N_{\text{sp}} = 611$ (70 per cent)
S0 galaxies in ATLAS <sup>3D</sup> ( $T > -3.5$ ):	$N_{\text{S0}} = 192$ (22 per cent)
E galaxies in ATLAS <sup>3D</sup> ( $T \leq -3.5$ ):	$N_E = 68$ (8 per cent)

complete. It ensures that all candidate galaxies brighter than an absolute total magnitude  $M_K = K_T - 5 \log D - 25 = -21.5 \text{ mag}$  are selected. This  $K_s$ -band luminosity limit roughly corresponds to a  $B$ -band selection  $M_B \lesssim -18 \text{ mag}$ , for the typical  $B - K_s \approx 3.5 \text{ mag}$  colour of ETGs, at the faint end of our selection. This criterion is thus again similar to the one in the SAURON survey and allows for a significant overlap in the samples, reducing the required observing time. This step provides a sample of  $\sim 20\,000$  extended objects classified as galaxies.

(v) Assign a distance to as many galaxies as possible in the selection and include in the ATLAS<sup>3D</sup> parent sample the ones with  $D < 42 \text{ Mpc}$  and  $M_K < -21.5 \text{ mag}$ . The distance selection requires some further explanation and may introduce incompleteness biases that are discussed in the next section.

A summary of the selection criteria is given in Table 1, while some of the main characteristics of the resulting galaxy sample are given in Table 2. This is the sample of galaxies, which includes both spiral and ETGs, from which the ATLAS<sup>3D</sup> sample of ETGs will be extracted. The names and the characteristics of the resulting 871 galaxies in the ATLAS<sup>3D</sup> parent sample are given in Tables 3 (for the ETGs) and 4 (for the spirals). As the evolution of spirals and ETGs are closely related, the spirals of the parent sample are critical to properly interpret the ATLAS<sup>3D</sup> results on ETGs.

### 2.2 Sources of distances and errors

Numerous sources of distances for nearby galaxies have been accumulated over the past decades. In most cases the distances are based on redshift as provided by large redshift surveys, but a number of more accurate distances are available based on other methods (see e.g. the recent compilations of Tully et al. 2008, 2009; Karachentsev & Nasonova 2010). For the  $\sim 20\,000$  2MASS galaxies with  $K_T < 11.6 \text{ mag}$  we tried to automatically assign the most accurate available distance according to the following order of priority.

(i) Distance obtained with the surface brightness fluctuation (SBF) method for the ACS Virgo Cluster Survey (Mei et al. 2007; Blakeslee et al. 2009) (91 values). These are claimed to be accurate to about 3 per cent in distance.

(ii) SBF distance from ground-based observation from Tonry et al. (2001) (300 values), which have a median error of 10 per cent in distance. These have been converted to the same zero-point of

**Table 3.** The ATLAS<sup>3D</sup> sample of 260 early-type (E and S0) galaxies. A machine-readable version of this table is available (see Supporting Information).

Galaxy	RA	Dec.	SBF	NED-D	Virgo	$V_{\text{hel}}$	$D$	$M_K$	$A_B$	$T$ type	$\log R_e$
(1)	( $^{\circ}$ )	( $^{\circ}$ )	(4)	(5)	(6)	( $\text{km s}^{-1}$ )	(Mpc)	(mag)	(mag)	(11)	(arcsec)
(1)	(2)	(3)	(4)	(5)	(6)	(7)	(8)	(9)	(10)	(11)	(12)
IC 0560	146.472656	-0.268221	0	0	0	1853	27.2	-22.10	0.59	-0.7	1.11
IC 0598	153.202423	43.145546	0	0	0	2256	35.3	-22.60	0.06	-0.1	1.02
IC 0676	168.165909	9.055736	0	0	0	1429	24.6	-22.27	0.11	-1.3	1.35
IC 0719	175.077042	9.009861	0	0	0	1833	29.4	-22.70	0.22	-2.0	1.10
IC 0782	185.404053	5.765672	0	0	0	2424	36.3	-22.02	0.09	2.7	1.35
IC 1024	217.863419	3.009107	0	0	0	1479	24.2	-21.85	0.13	-2.0	1.05
IC 3631	189.950195	12.973927	0	0	0	2822	42.0	-22.01	0.17	-1.3	1.13
NGC 0448	18.818876	-1.626105	1	1	0	1908	29.5	-23.02	0.26	-2.5	1.05
NGC 0474	20.027901	3.415270	0	1	0	2315	30.9	-23.91	0.15	-2.0	1.52
NGC 0502	20.731415	9.049169	0	0	0	2524	35.9	-23.05	0.17	-2.0	1.07
NGC 0509	20.850327	9.433469	0	0	0	2261	32.3	-21.89	0.20	-1.3	1.37
NGC 0516	21.033607	9.551668	0	0	0	2437	34.7	-22.21	0.29	-1.5	1.16
NGC 0524	21.198778	9.538793	1	10	0	2403	23.3	-24.71	0.36	-1.2	1.64
NGC 0525	21.220442	9.703240	0	0	0	2139	30.7	-21.86	0.38	-2.0	1.06
NGC 0661	26.060976	28.705988	0	1	0	3815	30.6	-23.19	0.30	-4.4	1.12
NGC 0680	27.447035	21.970827	0	1	0	2928	37.5	-24.17	0.34	-4.0	1.16
NGC 0770	29.806850	18.954695	0	0	0	2543	36.7	-22.57	0.31	-4.2	0.94
NGC 0821	32.088123	10.994870	1	4	0	1718	23.4	-23.99	0.48	-4.8	1.60
NGC 0936	36.906090	-1.156280	1	4	0	1429	22.4	-24.85	0.15	-1.2	1.72
NGC 1023	40.100052	39.063251	1	8	0	602	11.1	-24.01	0.26	-2.7	1.68
NGC 1121	42.663387	-1.734040	0	0	0	2558	35.3	-22.70	0.29	-1.8	0.87
NGC 1222	47.236446	-2.955212	0	0	0	2422	33.3	-22.71	0.26	-3.0	1.10
NGC 1248	48.202328	-5.224674	0	0	0	2217	30.4	-22.90	0.27	-2.0	1.20
NGC 1266	49.003120	-2.427370	0	0	0	2170	29.9	-22.93	0.43	-2.1	1.31
NGC 1289	49.707592	-1.973354	0	0	0	2792	38.4	-23.46	0.37	-2.1	1.26
NGC 1665	72.071098	-5.427655	0	0	0	2745	37.5	-23.63	0.26	-1.8	1.50
NGC 2481	119.307182	23.767693	0	0	0	2157	32.0	-23.38	0.28	0.4	1.02
NGC 2549	124.743111	57.803108	1	1	0	1051	12.3	-22.43	0.28	-2.0	1.28
NGC 2577	125.681137	22.553040	0	0	0	2062	30.8	-23.41	0.23	-3.0	1.15
NGC 2592	126.783669	25.970339	1	1	0	1979	25.0	-22.88	0.25	-4.8	1.09
NGC 2594	126.821609	25.878935	0	0	0	2362	35.1	-22.36	0.24	0.0	0.82
NGC 2679	132.887192	30.865419	0	0	0	2027	31.1	-22.81	0.14	-2.0	1.35
NGC 2685	133.894791	58.734409	0	0	0	875	16.7	-22.78	0.27	-1.0	1.41
NGC 2695	133.612778	-3.067101	1	3	0	1833	31.5	-23.64	0.08	-2.1	1.21
NGC 2698	133.902222	-3.183882	0	0	0	1900	27.1	-23.32	0.08	-1.0	1.10
NGC 2699	133.953415	-3.127507	1	3	0	1868	26.2	-22.72	0.08	-5.0	1.06
NGC 2764	137.072983	21.443447	0	0	0	2706	39.6	-23.19	0.17	-2.0	1.09
NGC 2768	137.906265	60.037209	1	5	0	1353	21.8	-24.71	0.20	-4.4	1.80
NGC 2778	138.101639	35.027424	1	1	0	2025	22.3	-22.23	0.09	-4.8	1.20
NGC 2824	139.759277	26.269999	0	0	0	2758	40.7	-22.93	0.14	-2.0	0.86
NGC 2852	140.810684	40.163879	0	0	0	1781	28.5	-22.18	0.06	1.0	0.85
NGC 2859	141.077286	34.513378	0	0	0	1690	27.0	-24.13	0.09	-1.2	1.43
NGC 2880	142.394241	62.490620	1	1	0	1554	21.3	-22.98	0.14	-2.7	1.32
NGC 2950	145.646317	58.851219	1	1	0	1322	14.5	-22.93	0.07	-2.0	1.19
NGC 2962	145.224609	5.165820	0	3	0	1967	34.0	-24.01	0.25	-1.1	1.39
NGC 2974	145.638611	-3.699116	1	3	0	1887	20.9	-23.62	0.23	-4.2	1.58
NGC 3032	148.034119	29.236279	1	2	0	1562	21.4	-22.01	0.07	-1.9	1.12
NGC 3073	150.216843	55.618935	1	1	0	1173	32.8	-21.78	0.05	-2.8	1.13
NGC 3098	150.569458	24.711092	0	0	0	1397	23.0	-22.72	0.16	-1.5	1.12
NGC 3156	153.171692	3.129320	1	3	0	1338	21.8	-22.15	0.15	-2.5	1.24
NGC 3182	154.887558	58.205818	0	0	0	2118	34.0	-23.19	0.05	0.4	1.32
NGC 3193	154.603683	21.893978	1	3	0	1381	33.1	-24.63	0.11	-4.8	1.42
NGC 3226	155.862549	19.898439	1	3	0	1315	22.9	-23.24	0.10	-4.8	1.49
NGC 3230	155.933090	12.567883	0	0	0	2795	40.8	-24.18	0.16	-1.8	1.26
NGC 3245	156.826523	28.507435	1	1	0	1326	20.3	-23.69	0.11	-2.1	1.40
NGC 3248	156.939270	22.847170	0	0	0	1481	24.6	-22.43	0.09	-2.0	1.20
NGC 3301	159.233459	21.882166	0	0	0	1339	22.8	-23.28	0.10	-0.4	1.30
NGC 3377	161.926666	13.985640	1	10	0	690	10.9	-22.76	0.15	-4.8	1.55
NGC 3379	161.956665	12.581630	1	15	0	918	10.3	-23.80	0.11	-4.8	1.60
NGC 3384	162.070404	12.629300	1	10	0	733	11.3	-23.52	0.12	-2.7	1.51
NGC 3400	162.689590	28.468929	0	0	0	1441	24.7	-21.82	0.08	0.7	1.23

Table 3 – *continued*

Galaxy	RA ( $^{\circ}$ )	Dec. ( $^{\circ}$ )	SBF	NED-D	Virgo	$V_{\text{hel}}$ ( $\text{km s}^{-1}$ )	$D$ (Mpc)	$M_K$ (mag)	$A_B$ (mag)	$T$ type	$\log R_e$ (arcsec)
(1)	(2)	(3)	(4)	(5)	(6)	(7)	(8)	(9)	(10)	(11)	(12)
NGC 3412	162.722137	13.412142	1	5	0	860	11.0	-22.55	0.12	-2.0	1.49
NGC 3414	162.817673	27.974968	1	1	0	1470	24.5	-23.98	0.11	-2.0	1.38
NGC 3457	163.702591	17.621157	1	1	0	1148	20.1	-21.89	0.13	-5.0	1.13
NGC 3458	164.006042	57.116970	0	0	0	1877	30.9	-23.12	0.04	-2.0	1.06
NGC 3489	165.077454	13.901258	1	5	0	695	11.7	-22.99	0.07	-1.2	1.35
NGC 3499	165.796280	56.221664	0	0	0	1535	26.4	-21.88	0.04	0.0	0.94
NGC 3522	166.668549	20.085621	0	1	0	1228	25.5	-21.67	0.10	-4.9	1.01
NGC 3530	167.168411	57.230160	0	0	0	1894	31.2	-22.00	0.04	0.0	0.87
NGC 3595	168.856461	47.447147	0	0	0	2177	34.7	-23.28	0.09	-3.3	1.15
NGC 3599	168.862305	18.110369	1	3	0	839	19.8	-22.22	0.09	-2.0	1.37
NGC 3605	169.194260	18.017141	1	3	0	661	20.1	-21.83	0.09	-4.5	1.23
NGC 3607	169.227737	18.051809	1	4	0	942	22.2	-24.74	0.09	-3.1	1.59
NGC 3608	169.245697	18.148531	1	4	0	1226	22.3	-23.65	0.09	-4.8	1.47
NGC 3610	169.605316	58.786247	1	4	0	1707	20.8	-23.69	0.04	-4.2	1.20
NGC 3613	169.650543	57.999924	1	3	0	2051	28.3	-24.26	0.05	-4.7	1.42
NGC 3619	169.840088	57.757683	0	0	0	1560	26.8	-23.57	0.08	-0.9	1.42
NGC 3626	170.015808	18.356791	1	1	0	1486	19.5	-23.30	0.08	-1.0	1.41
NGC 3630	170.070786	2.964170	0	0	0	1499	25.0	-23.16	0.18	-1.5	1.10
NGC 3640	170.278549	3.234764	1	4	0	1298	26.3	-24.60	0.19	-4.9	1.49
NGC 3641	170.286621	3.194489	1	1	0	1780	25.9	-21.85	0.18	-4.9	0.97
NGC 3648	170.631195	39.876972	0	0	0	1970	31.9	-23.06	0.09	-2.0	1.12
NGC 3658	170.992706	38.562424	0	0	0	2039	32.7	-23.45	0.09	-2.2	1.28
NGC 3665	171.181793	38.762791	0	0	0	2069	33.1	-24.92	0.08	-2.1	1.49
NGC 3674	171.610870	57.048290	0	0	0	2055	33.4	-23.23	0.06	-1.9	1.05
NGC 3694	172.225571	35.413857	0	0	0	2243	35.2	-22.35	0.10	-5.0	1.02
NGC 3757	174.261765	58.415649	0	0	0	1245	22.6	-22.15	0.06	-2.0	0.95
NGC 3796	175.129776	60.298958	0	0	0	1250	22.7	-21.84	0.06	0.0	1.06
NGC 3838	176.057205	57.948101	0	0	0	1308	23.5	-22.52	0.05	0.0	1.04
NGC 3941	178.230667	36.986378	1	2	0	930	11.9	-23.06	0.09	-2.0	1.40
NGC 3945	178.307190	60.675560	0	0	0	1281	23.2	-24.31	0.12	-1.2	1.45
NGC 3998	179.484039	55.453564	1	2	0	1048	13.7	-23.33	0.07	-2.1	1.30
NGC 4026	179.854950	50.961689	1	2	0	985	13.2	-23.03	0.09	-1.8	1.31
NGC 4036	180.362045	61.895699	0	0	0	1385	24.6	-24.40	0.10	-2.6	1.46
NGC 4078	181.198456	10.595537	0	0	0	2546	38.1	-22.99	0.11	-2.0	0.92
NGC 4111	181.763031	43.065392	1	1	0	792	14.6	-23.27	0.06	-1.4	1.08
NGC 4119	182.040176	10.378720	0	0	1	1656	16.5	-22.60	0.12	-1.3	1.60
NGC 4143	182.400360	42.534218	1	2	0	946	15.5	-23.10	0.05	-1.9	1.39
NGC 4150	182.640228	30.401487	1	4	0	208	13.4	-21.65	0.08	-2.1	1.20
NGC 4168	183.071808	13.205354	0	1	0	2286	30.9	-24.03	0.16	-4.8	1.48
NGC 4179	183.217087	1.299673	0	0	1	1300	16.5	-23.18	0.14	-1.9	1.30
NGC 4191	183.459915	7.200842	0	0	0	2646	39.2	-23.10	0.09	-1.8	1.06
NGC 4203	183.770935	33.197243	1	2	0	1087	14.7	-23.44	0.05	-2.7	1.47
NGC 4215	183.977142	6.401132	0	0	0	2011	31.5	-23.43	0.07	-0.9	1.18
NGC 4233	184.282043	7.624434	0	1	0	2306	33.9	-23.88	0.10	-2.0	1.19
NGC 4249	184.497650	5.598720	0	0	0	2618	38.7	-21.98	0.09	-1.3	1.10
NGC 4251	184.534607	28.175299	1	1	0	1066	19.1	-23.68	0.10	-1.9	1.29
NGC 4255	184.734100	4.785923	0	0	0	1995	31.2	-22.99	0.09	-1.9	1.10
NGC 4259	184.842468	5.376242	0	0	0	2497	37.2	-22.19	0.08	-2.0	0.89
NGC 4261	184.846924	5.824710	1	5	0	2212	30.8	-25.18	0.08	-4.8	1.58
NGC 4262	184.877426	14.877717	2	1	1	1375	15.4	-22.60	0.16	-2.7	1.10
NGC 4264	184.899078	5.846804	0	0	0	2518	37.5	-23.00	0.08	-1.1	1.14
NGC 4267	184.938675	12.798356	2	1	1	1021	15.8	-23.18	0.20	-2.7	1.58
NGC 4268	184.946762	5.283650	0	0	0	2034	31.7	-23.05	0.08	-0.3	1.20
NGC 4270	184.955978	5.463371	0	0	0	2331	35.2	-23.69	0.08	-2.0	1.21
NGC 4278	185.028320	29.280619	1	9	0	620	15.6	-23.80	0.13	-4.8	1.50
NGC 4281	185.089691	5.386430	0	1	0	2671	24.4	-24.01	0.09	-1.5	1.34
NGC 4283	185.086609	29.310898	1	3	0	1056	15.3	-21.80	0.11	-4.8	1.09
NGC 4324	185.775726	5.250488	0	0	1	1665	16.5	-22.61	0.10	-0.9	1.30
NGC 4339	185.895599	6.081713	1	3	1	1266	16.0	-22.49	0.11	-4.7	1.48
NGC 4340	185.897141	16.722195	0	2	1	933	18.4	-23.01	0.11	-1.2	1.57
NGC 4342	185.912598	7.053936	0	0	1	761	16.5	-22.07	0.09	-3.4	0.82

Table 3 – continued

Galaxy	RA (°)	Dec. (°)	SBF	NED-D	Virgo	$V_{\text{hel}}$ (km s <sup>-1</sup> )	$D$ (Mpc)	$M_K$ (mag)	$A_B$ (mag)	$T$ type	$\log R_e$ (arcsec)
(1)	(2)	(3)	(4)	(5)	(6)	(7)	(8)	(9)	(10)	(11)	(12)
NGC 4346	185.866425	46.993881	1	1	0	832	13.9	-22.55	0.05	-2.0	1.29
NGC 4350	185.990891	16.693356	0	2	1	1210	15.4	-23.13	0.12	-1.8	1.23
NGC 4365	186.117615	7.317520	2	13	0	1243	23.3	-25.21	0.09	-4.8	1.72
NGC 4371	186.230957	11.704288	2	1	1	933	17.0	-23.45	0.16	-1.3	1.47
NGC 4374	186.265747	12.886960	2	13	1	1017	18.5	-25.12	0.18	-4.3	1.72
NGC 4377	186.301285	14.762218	2	1	1	1338	17.8	-22.43	0.17	-2.6	1.13
NGC 4379	186.311386	15.607498	2	2	1	1074	15.8	-22.24	0.10	-2.8	1.27
NGC 4382	186.350220	18.191080	2	7	1	746	17.9	-25.13	0.13	-1.3	1.82
NGC 4387	186.423813	12.810359	2	3	1	565	17.9	-22.13	0.14	-4.9	1.20
NGC 4406	186.549225	12.945970	2	15	1	-224	16.8	-25.04	0.13	-4.8	1.97
NGC 4417	186.710938	9.584117	2	1	1	828	16.0	-22.86	0.11	-1.9	1.25
NGC 4425	186.805664	12.734803	0	0	1	1908	16.5	-22.09	0.13	-0.6	1.38
NGC 4429	186.860657	11.107540	0	0	1	1104	16.5	-24.32	0.14	-1.1	1.62
NGC 4434	186.902832	8.154311	2	5	0	1070	22.4	-22.55	0.10	-4.8	1.16
NGC 4435	186.918762	13.079021	2	0	1	791	16.7	-23.83	0.13	-2.1	1.49
NGC 4442	187.016220	9.803620	2	1	1	547	15.3	-23.63	0.09	-1.9	1.44
NGC 4452	187.180417	11.755000	0	2	1	188	15.6	-21.88	0.13	-2.0	1.30
NGC 4458	187.239716	13.241916	2	8	1	677	16.4	-21.76	0.10	-4.8	1.37
NGC 4459	187.250107	13.978580	2	3	1	1192	16.1	-23.89	0.19	-1.4	1.56
NGC 4461	187.262543	13.183857	0	0	1	1924	16.5	-23.08	0.10	-0.8	1.40
NGC 4472	187.444992	8.000410	2	18	1	981	17.1	-25.78	0.10	-4.8	1.98
NGC 4473	187.453659	13.429320	2	8	1	2260	15.3	-23.77	0.12	-4.7	1.43
NGC 4474	187.473099	14.068673	2	1	1	1611	15.6	-22.28	0.18	-2.0	1.30
NGC 4476	187.496170	12.348669	2	3	1	1968	17.6	-21.78	0.12	-3.0	1.20
NGC 4477	187.509048	13.636443	0	0	1	1338	16.5	-23.75	0.14	-1.9	1.59
NGC 4478	187.572662	12.328578	2	9	1	1375	17.0	-22.80	0.10	-4.8	1.20
NGC 4483	187.669250	9.015665	2	1	1	906	16.7	-21.84	0.09	-1.3	1.24
NGC 4486	187.705933	12.391100	2	15	1	1284	17.2	-25.38	0.10	-4.3	1.91
NGC 4486A	187.740540	12.270361	2	0	1	758	18.3	-21.82	0.10	-5.0	0.94
NGC 4489	187.717667	16.758696	2	5	1	961	15.4	-21.59	0.12	-4.8	1.42
NGC 4494	187.850143	25.774981	1	9	0	1342	16.6	-24.11	0.09	-4.8	1.69
NGC 4503	188.025803	11.176434	0	0	1	1334	16.5	-23.22	0.22	-1.8	1.45
NGC 4521	188.198853	63.939293	0	0	0	2511	39.7	-23.92	0.08	-0.1	1.21
NGC 4526	188.512619	7.699140	1	5	1	617	16.4	-24.62	0.10	-1.9	1.65
NGC 4528	188.525269	11.321266	2	0	1	1378	15.8	-22.05	0.20	-2.0	1.15
NGC 4546	188.872940	-3.793227	1	2	0	1057	13.7	-23.30	0.15	-2.7	1.40
NGC 4550	188.877548	12.220955	2	3	1	459	15.5	-22.27	0.17	-2.1	1.19
NGC 4551	188.908249	12.264010	2	5	1	1176	16.1	-22.18	0.17	-4.9	1.22
NGC 4552	188.916183	12.556040	2	12	1	344	15.8	-24.29	0.18	-4.6	1.53
NGC 4564	189.112473	11.439320	2	5	1	1155	15.8	-23.08	0.14	-4.8	1.31
NGC 4570	189.222504	7.246663	2	1	1	1787	17.1	-23.48	0.09	-2.0	1.30
NGC 4578	189.377274	9.555121	2	3	1	2292	16.3	-22.66	0.09	-2.0	1.51
NGC 4596	189.983063	10.176031	0	0	1	1892	16.5	-23.63	0.09	-0.9	1.59
NGC 4608	190.305374	10.155793	0	0	1	1850	16.5	-22.94	0.07	-1.9	1.42
NGC 4612	190.386490	7.314782	2	1	1	1775	16.6	-22.55	0.11	-2.0	1.40
NGC 4621	190.509674	11.646930	2	9	1	467	14.9	-24.14	0.14	-4.8	1.63
NGC 4623	190.544601	7.676934	2	1	1	1807	17.4	-21.74	0.10	-1.5	1.31
NGC 4624	191.274826	3.055684	0	0	1	912	16.5	-23.67	0.10	-0.6	1.64
NGC 4636	190.707779	2.687780	1	11	0	930	14.3	-24.36	0.12	-4.8	1.95
NGC 4638	190.697632	11.442459	2	2	1	1152	17.5	-23.01	0.11	-2.7	1.22
NGC 4643	190.833893	1.978399	0	0	1	1333	16.5	-23.69	0.13	-0.6	1.38
NGC 4649	190.916702	11.552610	2	11	1	1110	17.3	-25.46	0.11	-4.6	1.82
NGC 4660	191.133209	11.190533	2	5	1	1087	15.0	-22.69	0.15	-4.7	1.09
NGC 4684	191.822861	-2.727538	1	1	0	1560	13.1	-22.21	0.12	-1.2	1.32
NGC 4690	191.981323	-1.655975	0	0	0	2765	40.2	-22.96	0.13	-3.0	1.25
NGC 4694	192.062881	10.983624	0	0	1	1171	16.5	-22.15	0.17	-2.0	1.47
NGC 4697	192.149612	-5.800850	1	8	0	1252	11.4	-23.93	0.13	-4.4	1.79
NGC 4710	192.412323	15.165490	0	0	1	1102	16.5	-23.53	0.13	-0.9	1.48
NGC 4733	192.778259	10.912103	1	1	1	925	14.5	-21.80	0.09	-3.8	1.52
NGC 4753	193.092133	-1.199690	1	3	0	1163	22.9	-25.09	0.14	-1.4	1.69
NGC 4754	193.073181	11.313660	2	3	1	1351	16.1	-23.64	0.14	-2.5	1.50
NGC 4762	193.233536	11.230800	0	2	0	986	22.6	-24.48	0.09	-1.8	1.64

Table 3 – *continued*

Galaxy	RA ( $^{\circ}$ )	Dec. ( $^{\circ}$ )	SBF	NED-D	Virgo	$V_{\text{hel}}$ ( $\text{km s}^{-1}$ )	$D$ (Mpc)	$M_K$ (mag)	$A_B$ (mag)	$T$ type	$\log R_e$ (arcsec)
(1)	(2)	(3)	(4)	(5)	(6)	(7)	(8)	(9)	(10)	(11)	(12)
NGC 4803	193.890289	8.240547	0	0	0	2645	39.4	-22.28	0.13	0.0	0.94
NGC 5103	200.125229	43.084015	0	0	0	1273	23.4	-22.36	0.08	0.0	1.02
NGC 5173	202.105301	46.591572	0	0	0	2424	38.4	-22.88	0.12	-4.9	1.01
NGC 5198	202.547546	46.670830	0	0	0	2519	39.6	-24.10	0.10	-4.8	1.38
NGC 5273	205.534943	35.654240	1	2	0	1085	16.1	-22.37	0.04	-1.9	1.57
NGC 5308	206.751633	60.973038	0	6	0	1998	31.5	-24.13	0.08	-2.1	1.25
NGC 5322	207.313339	60.190411	1	5	0	1780	30.3	-25.26	0.06	-4.8	1.60
NGC 5342	207.857910	59.863014	0	0	0	2189	35.5	-22.61	0.05	-2.0	0.97
NGC 5353	208.361420	40.283123	0	0	0	2198	35.2	-25.11	0.05	-2.1	1.30
NGC 5355	208.439850	40.338795	0	0	0	2344	37.1	-22.40	0.05	-2.1	1.06
NGC 5358	208.501801	40.277420	0	0	0	2412	38.0	-22.01	0.04	-0.2	1.05
NGC 5379	208.893112	59.742825	0	0	0	1774	30.0	-22.08	0.08	-2.0	1.32
NGC 5422	210.175262	55.164478	0	0	0	1838	30.8	-23.69	0.06	-1.5	1.33
NGC 5473	211.180176	54.892620	0	0	0	2022	33.2	-24.25	0.05	-2.7	1.32
NGC 5475	211.301437	55.741802	0	0	0	1671	28.6	-22.88	0.05	1.0	1.22
NGC 5481	211.671722	50.723320	0	2	0	1989	25.8	-22.68	0.08	-3.9	1.35
NGC 5485	211.797134	55.001518	1	3	0	1927	25.2	-23.61	0.07	-2.0	1.45
NGC 5493	212.872421	-5.043663	0	0	0	2665	38.8	-24.49	0.15	-2.1	1.14
NGC 5500	212.563522	48.546066	0	0	0	1914	31.7	-21.93	0.09	-4.9	1.18
NGC 5507	213.332825	-3.148860	0	0	0	1851	28.5	-23.19	0.26	-2.3	1.09
NGC 5557	214.607117	36.493690	0	3	0	3219	38.8	-24.87	0.03	-4.8	1.46
NGC 5574	215.233109	3.237995	1	1	0	1589	23.2	-22.30	0.13	-2.8	1.13
NGC 5576	215.265381	3.271049	1	3	0	1506	24.8	-24.15	0.13	-4.8	1.34
NGC 5582	215.179703	39.693584	1	3	0	1430	27.7	-23.28	0.06	-4.9	1.44
NGC 5611	216.019897	33.047501	1	1	0	1968	24.5	-22.20	0.05	-1.9	1.00
NGC 5631	216.638687	56.582664	1	1	0	1944	27.0	-23.70	0.09	-1.9	1.32
NGC 5638	217.418289	3.233443	1	3	0	1652	25.6	-23.80	0.14	-4.8	1.45
NGC 5687	218.718201	54.475685	1	1	0	2143	27.2	-23.22	0.05	-3.0	1.36
NGC 5770	223.312653	3.959721	1	1	0	1471	18.5	-22.15	0.17	-2.0	1.23
NGC 5813	225.296936	1.701970	1	4	0	1956	31.3	-25.09	0.25	-4.8	1.76
NGC 5831	226.029266	1.219917	1	3	0	1645	26.4	-23.69	0.25	-4.8	1.40
NGC 5838	226.359467	2.099356	0	0	0	1341	21.8	-24.13	0.23	-2.6	1.40
NGC 5839	226.364471	1.634633	1	1	0	1220	22.0	-22.53	0.23	-2.0	1.22
NGC 5845	226.503281	1.633824	1	2	0	1472	25.2	-22.92	0.23	-4.9	0.80
NGC 5846	226.621887	1.605637	1	6	0	1712	24.2	-25.01	0.24	-4.7	1.77
NGC 5854	226.948853	2.568560	0	0	0	1663	26.2	-23.30	0.23	-1.1	1.26
NGC 5864	227.389786	3.052741	0	0	0	1874	29.0	-23.62	0.19	-1.7	1.35
NGC 5866	226.623169	55.763309	1	3	0	755	14.9	-24.00	0.06	-1.3	1.56
NGC 5869	227.456055	0.469967	0	1	0	2065	24.9	-23.27	0.24	-2.3	1.31
NGC 6010	238.579773	0.543033	0	0	0	2022	30.6	-23.53	0.45	0.4	1.16
NGC 6014	238.989105	5.931838	0	0	0	2381	35.8	-22.99	0.22	-1.9	1.35
NGC 6017	239.314529	5.998364	1	1	0	1788	29.0	-22.52	0.23	-5.0	0.85
NGC 6149	246.851151	19.597290	0	0	0	2427	37.2	-22.60	0.30	-1.9	1.03
NGC 6278	255.209763	23.010956	0	0	0	2832	42.9	-24.19	0.27	-1.9	1.22
NGC 6547	271.291748	25.232645	0	0	0	2677	40.8	-23.60	0.50	-1.3	1.06
NGC 6548	271.496826	18.587217	1	1	0	2208	22.4	-23.19	0.35	-1.9	1.35
NGC 6703	281.828522	45.550648	1	4	0	2373	25.9	-23.85	0.37	-2.8	1.34
NGC 6798	291.013306	53.624752	0	0	0	2360	37.5	-23.52	0.57	-2.0	1.23
NGC 7280	336.614899	16.148266	1	2	0	1845	23.7	-22.83	0.24	-1.3	1.33
NGC 7332	339.352173	23.798351	1	1	0	1197	22.4	-23.75	0.16	-1.9	1.24
NGC 7454	345.277130	16.388371	1	3	0	2020	23.2	-23.00	0.33	-4.7	1.41
NGC 7457	345.249725	30.144892	1	3	0	844	12.9	-22.38	0.23	-2.6	1.56
NGC 7465	345.503967	15.964876	0	0	0	1960	29.3	-22.82	0.33	-1.9	0.90
NGC 7693	353.293671	-1.292010	0	0	0	2502	35.4	-21.58	0.15	-1.0	1.11
NGC 7710	353.942261	-2.880941	0	0	0	2407	34.0	-21.99	0.15	-1.9	0.92
PGC 016060	72.143387	-3.867104	0	0	0	2764	37.8	-22.64	0.19	-0.6	1.01
PGC 028887	149.931290	11.660812	0	0	0	2833	41.0	-22.26	0.17	0.0	1.08
PGC 029321	151.463226	12.961213	0	0	0	2816	40.9	-21.66	0.16	0.0	0.89
PGC 035754	173.614716	33.178913	0	0	0	2534	39.0	-21.90	0.11	-3.0	0.83
PGC 042549	190.316513	-5.009177	0	0	0	2822	40.7	-22.71	0.11	-5.0	1.06
PGC 044433	194.578110	13.391409	0	0	0	2675	40.1	-22.25	0.13	0.0	0.71
PGC 050395	211.913544	54.794575	0	0	0	2322	37.2	-21.92	0.05	0.0	1.04

Table 3 – continued

Galaxy	RA (°)	Dec. (°)	SBF	NED-D	Virgo	$V_{\text{hel}}$ (km s <sup>-1</sup> )	$D$ (Mpc)	$M_K$ (mag)	$A_B$ (mag)	$T$ type	log $R_e$ (arcsec)
(1)	(2)	(3)	(4)	(5)	(6)	(7)	(8)	(9)	(10)	(11)	(12)
PGC 051753	217.310318	44.699104	0	0	0	2418	38.3	-21.92	0.05	0.0	1.01
PGC 054452	228.894180	2.248187	0	0	0	1918	29.5	-21.59	0.18	-2.0	1.14
PGC 056772	240.548340	7.085953	0	0	0	2655	39.5	-22.06	0.19	-2.0	0.93
PGC 058114	246.517838	2.906550	0	0	0	1507	23.8	-21.57	0.29	-2.0	0.97
PGC 061468	272.360748	19.117682	0	0	0	2371	36.2	-21.68	0.35	0.0	1.06
PGC 071531	352.121338	19.863962	0	0	0	2030	30.4	-21.74	0.53	-4.0	0.88
PGC 170172	176.731720	-5.187745	0	0	0	2562	37.1	-21.89	0.08	-5.0	0.89
UGC 03960	115.094856	23.275089	0	0	0	2255	33.2	-21.89	0.20	-4.9	1.24
UGC 04551	131.024582	49.793968	0	0	0	1728	28.0	-22.92	0.10	-2.0	1.03
UGC 05408	150.966095	59.436138	0	0	0	2998	45.8	-22.03	0.06	-3.3	0.84
UGC 06062	164.656662	9.050468	0	0	0	2634	38.7	-22.82	0.13	-2.0	1.05
UGC 06176	166.852753	21.657185	0	0	0	2677	40.1	-22.66	0.08	-2.0	1.03
UGC 08876	209.241943	45.973179	0	0	0	2085	33.9	-22.37	0.04	-0.1	0.93
UGC 09519	221.588028	34.370651	0	0	0	1631	27.6	-21.98	0.09	-1.9	0.87

Note. Column (1): the name is the principal designation from LEDA, which is used as standard designation for our project. Column (2): right Ascension in degrees and decimal (J2000.0). Column (3): declination in degrees and decimals (J2000.0). As the galaxy names may not be always consistent between different catalogues, these coordinate *define* the galaxies of the sample. Column (4): SBF = 1 if the galaxy is in Tonry et al. (2001) and SBF = 2 if it is in Mei et al. (2007) or both. Column (5): number of redshift-independent distance determinations listed in the NED-D catalogue, excluding the ones based on kinematical scaling relations. Column (6): Virgo = 1 if the galaxies is contained within a sphere of radius  $R = 3.5$  Mpc from the centre of the cluster assumed at coordinates RA =  $12^{\text{h}}28^{\text{m}}19^{\text{s}}$  and Dec. =  $+12^{\circ}40'$  (Mould et al. 2000) and distance  $D = 16.5$  Mpc (Mei et al. 2007). Column (7): heliocentric velocity measured from the SAURON integral field stellar kinematics ( $1\sigma$  error  $\Delta V_{\text{hel}} = 5$  km s<sup>-1</sup>). Column (8): distance in Mpc; when SBF = 1 the distance comes from Tonry et al. (2001), corrected by *subtracting* 0.06 mag to the distance modulus (Mei et al. 2007); when SBF = 2 the distance comes from Mei et al. (2007); when SBF = 0 and NED-D > 0 the distance is the median of the NED-D values, excluding the ones based on kinematical scaling relations; when SBF = NED-D = 0 and the galaxy is in Virgo (Virgo = 1) then it is assigned the cluster distance  $D = 16.5$  Mpc (Mei et al. 2007); otherwise  $D = V_{\text{cosmic}}/H_0$ , with  $H_0 = 72$  km s<sup>-1</sup> Mpc<sup>-1</sup>, where  $V_{\text{cosmic}}$  is the velocity derived from  $V_{\text{hel}}$  via the local flow field model of Mould et al. (2000) using only the Virgo attractor. Column (9): total galaxy absolute magnitude derived from the apparent magnitude  $K_T$  (2MASS keyword k\_m\_ext) at the adopted distance  $D$  and corrected for the foreground galactic extinction:  $M_K = K_T - 5 \log_{10} D - 25 - A_B/11.8$ , which assumes  $A_B/A_K = 11.8$ . Column (10):  $B$ -band foreground galactic extinction from Schlegel, Finkbeiner & Davis (1998). Column (11): morphological  $T$  type from HyperLeda. E:  $T \leq -3.5$ ; S0:  $-3.5 < T \leq -0.5$ . This morphology was *not* the one used for the sample selection, but is printed in Figs 5 and 6. Column (12): projected half-light effective radius. It was derived from a combination of RC3 and 2MASS determinations, which both use growth curves, as described in Section 4.1, but it was normalized to agree on average with RC3.

Table 4. The 611 spiral galaxies in the ATLAS<sup>3D</sup> parent sample.

Galaxy	RA (°)	Dec. (°)	SBF	NED-D	Virgo	$V_{\text{hel}}$ (km s <sup>-1</sup> )	$D$ (Mpc)	$M_K$ (mag)	$A_B$ (mag)	$T$ type	log $R_e$ (arcsec)
(1)	(2)	(3)	(4)	(5)	(6)	(7)	(8)	(9)	(10)	(11)	(12)
IC 0065	15.230966	47.681984	0	0	0	2614	39.7	-23.54	0.64	4.0	1.38
IC 0163	27.312431	20.711317	0	0	0	2749	39.7	-22.38	0.36	8.0	1.35
IC 0239	39.116250	38.970000	0	0	0	903	15.7	-22.23	0.31	6.0	1.90
IC 0540	142.542755	7.902529	0	0	0	2035	30.0	-21.89	0.26	3.5	1.08
IC 0591	151.865479	12.274520	0	0	0	2839	41.2	-21.82	0.15	6.0	1.19
IC 0610	156.618179	20.228252	0	0	0	1170	19.6	-21.53	0.09	3.9	1.02
IC 0750	179.717606	42.722404	0	1	0	701	36.8	-24.71	0.09	2.1	1.24
IC 0777	184.849228	28.309881	0	0	0	2541	39.0	-21.92	0.10	2.6	0.95
IC 0800	188.486313	15.354542	0	0	0	2326	35.8	-22.20	0.16	5.2	1.56
IC 0851	197.143127	21.049742	0	0	0	2615	39.8	-21.82	0.15	3.1	1.31

Note. The meaning of the columns is the same as in Table 3, except for column (7), which contain here the heliocentric velocity taken from NED. Only the first 10 rows are shown; the full 611 will be published electronically (see Supporting Information). Both Tables 3 and 4 are available from our project website <http://purl.org/atlas3d>

Mei et al. (2007) by subtracting 0.06 mag to the distance moduli (see discussion in Blakeslee et al. 2010).

(iii) Distances from the NED-D compilation<sup>1</sup> by Madore, Steer and the NED team (V3.0 June 2010, about 2000 values). The list includes accurate determinations using (1) SBF, (2) the tip of the red giant branch (TRGB), (3) Cepheids variables, with a claimed com-

parable accuracy of  $\sim 10$  per cent, but the list also includes various other methods like the ones based on the (4) Tully & Fisher (1977) or (5) Fundamental Plane (Djorgovski & Davis 1987; Dressler et al. 1987) relations, on the (6) luminosity of Type Ia Supernovae, or on the luminosity functions of (7) globular clusters and (8) planetary nebulae. The latter methods are expected to be accurate to better than  $\lesssim 20$  per cent (Tully et al. 2008). For a number of galaxies more than one independent distance was available and we adopted the median of the values.

<sup>1</sup> <http://nedwww.ipac.caltech.edu/Library/Distances/>

(iv) When no better distance was available, for galaxies within  $12^\circ$  of the projected centre of the Virgo cluster (defined by the galaxy M87) with heliocentric radial velocities  $V_{\text{hel}} < 2300 \text{ km s}^{-1}$ , we assigned the distance of the cluster (assumed to be 16.5 Mpc from Mei et al. 2007). These distances should be accurate to  $\sim 7$  per cent, considering the intrinsic depth of the cluster. Two galaxies were later removed from Virgo as that distance implied a too high and non-physical dynamical  $M/L$  as determined in Cappellari et al. (2010).

(v) Finally, if none of the above criteria was met, we assigned a distance based on the observed heliocentric radial velocities  $V_{\text{hel}}$ , which we converted to velocities  $V_{\text{cosmic}}$  characteristic of the expansion of the universe following Mould et al. (2000),<sup>2</sup> but only including the contribution of the Virgo attractor, and assuming  $H_0 = 72 \text{ km s}^{-1} \text{ Mpc}^{-1}$  (Dunkley et al. 2009). We repeated our sample selection using heliocentric velocities extracted from either the HyperLeda<sup>3</sup> (Paturel et al. 2003) or NED<sup>4</sup> data bases and obtained identical final ATLAS<sup>3D</sup> samples. We compared the  $V_{\text{hel}}$  of galaxies from NED and HyperLeda and found a general very good agreement in the two data bases, with a biweight rms scatter of 0.4 per cent, as expected given that in most cases the redshifts come from the same source. However in some cases significant differences exist: we found 83/5398 galaxies (1.5 per cent) with  $V_{\text{hel}}$  differences larger than 20 per cent. For our  $V_{\text{hel}}$  in the parent sample we adopted NED (2010 June), which currently includes as major sources the Center for Astrophysics Redshift Catalog (Huchra et al. 1983), the RC3 (de Vaucouleurs et al. 1991), the ZCAT compilation (Huchra et al. 1992) and the Sloan Digital Sky Survey DR7 (Abazajian et al. 2009). After obtaining our new accurate SAURON redshifts (Section 4.3) we updated the redshift-based distances and this led to the removal of one observed galaxy. However, we retained in the sample two observed galaxies formally with  $D > 42 \text{ Mpc}$ , but still inside our volume within the distance errors.

To estimate the representative errors of the redshift distances we correlated them against the direct distance estimates in the NED-D compilation. Specifically we selected the 285 galaxies in common with our sample with at least three independent distance determinations (in most cases including SBF distances), and we correlated the median of their  $d_{\text{NED-D}} \times H_0$  values against the  $V_{\text{cosmic}}$  (Fig. 1). We found a biweight dispersion of 24 per cent in the residuals. The minimum value in the median residual was obtained with  $H_0 = 72 \text{ km s}^{-1} \text{ Mpc}^{-1}$ , consistent with the adopted *Wilkinson Microwave Anisotropy Probe* estimate. Assuming a typical rms error of 10 per cent for the best set of NED-D distances, this implies an intrinsic rms error of  $\sim 21$  per cent in the redshift distances. However, a significant number of outliers exist. If we repeat the comparison for all the 692 galaxies in common, with a NED-D distance, the biweight dispersion increases to 29 per cent, which would imply a redshift error of  $\sim 27$  per cent. If we only consider the Local Group's peculiar velocity into Virgo in the calculation of  $V_{\text{cosmic}}$ , the scatter increases significantly and systematic deviations appear. Including the infall of galaxies into the Virgo attractor improves the agreement. However including other attractors as done by Mould et al. (2000) does not appear to further reduce the scatter. For this reason we only included the more secure Virgo attractor contribution in our redshift distances corrections.

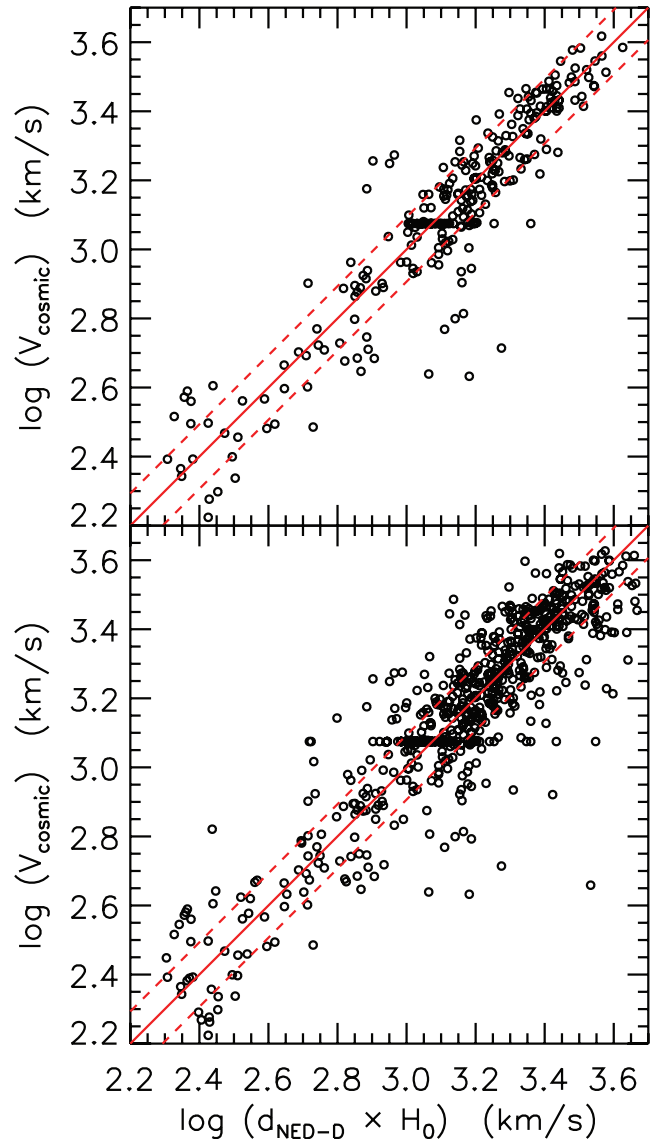


**Figure 1.** Accuracy of redshift distances. Top panel: recession velocities, converted into velocities  $V_{\text{cosmic}}$  characteristic of the expansion of the universe, against the median of the NED-D redshift-independent distances for 291 galaxies with at least three independent determination (in most cases including SBF distances). The solid line is a one-to-one relation, while the dashed lines indicate  $\pm 24$  per cent deviations. Bottom panel: same as in the top panel for 705 galaxies with at least one distance determination in NED-D.

### 2.3 Estimating redshift incompleteness

Not all the  $\sim 20\,000$  2MASS galaxies satisfying our observability criteria and with  $K_T < 11.6$  mag have a redshift measurement. This may introduce biases in our volume-limited sample selection. Specifically 4146/14461 (29 per cent) of the galaxies in the faintest magnitude bin  $10.6 < K_T < 11.6$  mag do not have a redshift in NED.<sup>5</sup> The redshift completeness quickly improves for brighter apparent magnitudes, and in fact only 4 per cent of the galaxies

<sup>2</sup> Corrected as described in the corresponding erratum.

<sup>3</sup> <http://leda.univ-lyon1.fr/>

<sup>4</sup> <http://nedwww.ipac.caltech.edu/>

<sup>5</sup> The situation will change in the near future when the 2MASS Redshift Survey will become available, which is already complete down to  $K_s = 11.25$  (Crook et al. 2007) and ultimately aims for a redshift completeness down to  $K_s = 13.0$  (Huchra et al. 2005).

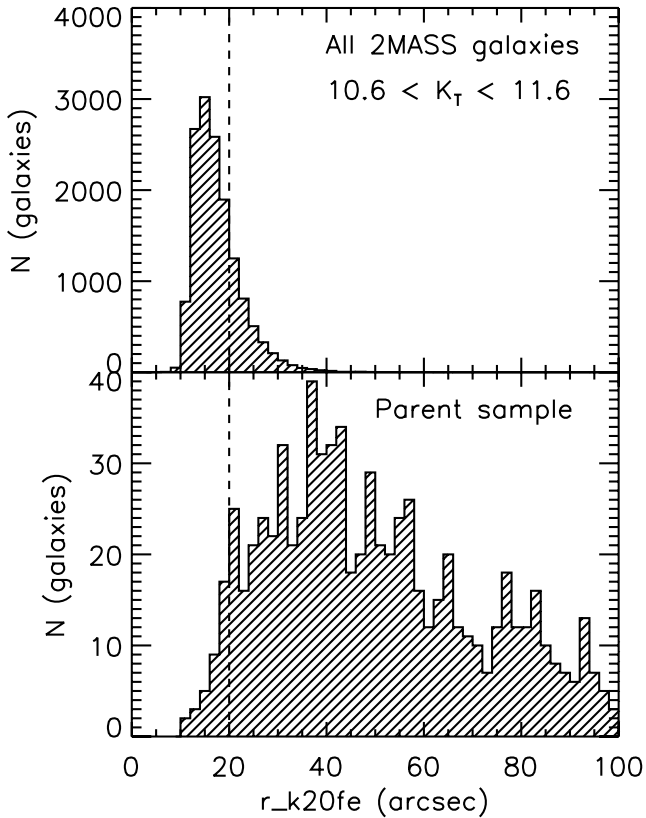


**Figure 2.** Apparent size distribution of 2MASS galaxies. Top panel: the apparent size, as described by the 2MASS XSC parameter  $r_{k20fe}$ , for all the galaxies satisfying our observability criteria and with  $10.6 < K_T < 11.6$ . Bottom panel: same as in the top panel for the galaxies in the parent sample ( $D < 42$  Mpc and  $M_K < -21.5$  mag).

with  $K_T < 10.6$  mag have no redshift. One way to estimate how many of these galaxies are likely to be within our selection criteria is to look at their size distribution as measured by 2MASS. In fact one expects many of the apparently faint and small galaxies to be intrinsically brighter and larger, but to appear faint and small due to the large distance.

To quantify the galaxy angular sizes we use the 2MASS XSC parameter  $r_{k20fe}$ , which gives the semimajor axis of the 20 mag arcsec<sup>-2</sup> surface brightness isophote at  $K_s$ . The size distribution for the galaxies in the faintest magnitude bin, according to this size parameter is shown in the top panel of Fig. 2. As expected the distribution presents a dramatic increase in the numbers for very small objects. For comparison we show in the bottom panel the size distribution of the 2MASS galaxies which satisfy our selection criteria  $D < 42$  Mpc and  $M_K < -21.5$  mag. The latter sample has a peak in the size distribution around  $r_{k20fe} \approx 40$  arcsec, while the number of objects sharply drops for  $r_{k20fe} \lesssim 20$  arcsec (only 4 per cent of the objects have sizes below that limit). This lack of apparently small objects is not due to any redshift selection criteria. In fact among all the galaxies with measured redshift, about equal numbers have size larger or smaller than  $r_{k20fe} = 20$  arcsec. The apparent galaxy size is just an efficient way to select, without redshift information, galaxies unlikely to belong to our volume-limited sample.

Excluding all objects apparently smaller than  $r_{k20fe} < 20$  arcsec, likely outside the limits of our local volume, we find a redshift incompleteness of 478/3383 (14 per cent) in the faintest

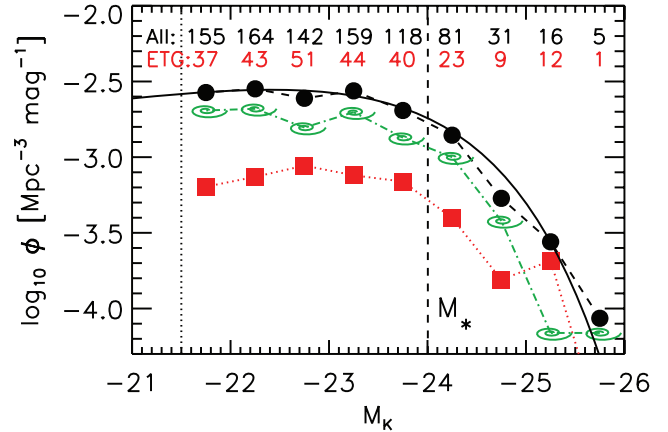


**Figure 3.**  $K_s$ -band luminosity function (LF) of the ATLAS<sup>3D</sup> parent sample of 871 galaxies (black filled circles). The LF for the spiral galaxies (green spirals) and the 260 ETGs which constitute the ATLAS<sup>3D</sup> sample (red squares) separately are also shown. The solid curve shows the Schechter (1976) function derived by Bell et al. (2003) from a fit to 6282 galaxies. It was not fitted to our data! The black numbers above the symbols indicate the total number of galaxies included in each 0.5-mag bin, while the red ones are the corresponding numbers for the ETGs of the ATLAS<sup>3D</sup> sample. There is no evidence of incompleteness down to the magnitude limit of the survey (vertical dotted line), which is  $\approx 2.5$  mag below  $M_*$  (vertical dashed line).

magnitude bin. Among the galaxies that *do* have redshift in this set, only 68/2905 (2 per cent) satisfy the selection criteria for the parent sample (most of the others are still outside the local volume). This implies that statistically we may expect  $\sim 11$  galaxies (1 per cent of the parent sample) to be possibly missed from the parent sample due to redshift incompleteness in the faintest magnitude bin. We conclude that we can safely ignore this possible bias from any conclusion derived from the sample.

## 2.4 Luminosity function

The ATLAS<sup>3D</sup> parent sample was carefully selected to provide a volume-limited sample of galaxies in the nearby universe. It should be representative of the galaxy population at low redshift, apart from the unavoidable cosmic variance, due to the relatively limited size of the volume. A first test of the representativeness of our parent sample is to compare its  $K_s$ -band luminosity function against that measured from larger volumes. For this we compare in Fig. 3 the luminosity function of the parent sample against that derived from a much larger sample, at a mean redshift  $\langle z \rangle \approx 0.08$ , by Bell et al. (2003), using 2MASS  $K_s$ -band photometry as we do, and SDSS redshifts. It agrees well with the ones by Kochanek et al. (2001) and Cole et al. (2001). The comparison shows excellent agreement between the two luminosity functions, both in shape and normalization, and indicates that our parent sample is representative of the general galaxy population. In particular this test shows no sign of incompleteness at the faint end, in agreement with the discussion of Section 2.3.

## 2.5 Size–luminosity relations for spirals and ETGs

To illustrate the general characteristic of the galaxies in the parent sample Fig. 4 shows the  $K$ -band size–luminosity relation and the effective surface brightness  $\Sigma_{50} \equiv L_{\odot K} / (2\pi R_e^2)$  for different morphological types. This plot shows a similar distribution as the

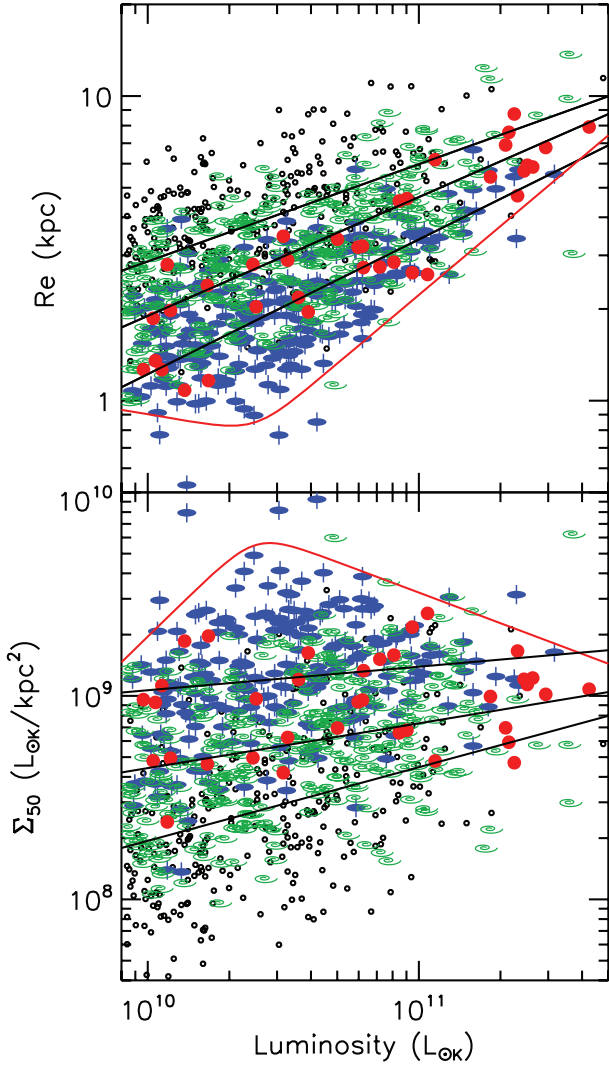


**Figure 4.** Top panel: size–luminosity relation for the parent sample. The  $K$ -band luminosity of all the galaxies in the parent sample is plotted against the effective radius  $R_e$  (Section 4.1). Red filled circles are slow rotators, blue ellipses with vertical axis are fast rotators. These 260 objects constitute the ATLAS<sup>3D</sup> sample. The green spirals represent spiral galaxies of type Sa–Sb ( $-0.5 < T \leq 4$ ), while later spiral types ( $T > 4$ ) are plotted as small open circles. The solid lines are the best-fitting relations described in the text. From the bottom to the top they are fit to the fast rotators ETGs, to the Sa–Sb and to the later spiral types. The red curve approximates the boundary of the zone of avoidance in the observed galaxy distribution. Bottom panel: effective surface brightness versus luminosity. The symbols and the lines are the same as in the top panel.

one inferred from much larger galaxy samples based on SDSS photometry, further confirming the representativeness of our sample (compare Fig. 4 with fig. 2 of van Dokkum et al. 2008). In our plot we show the fast/slow rotator classification for the 260 ETGs of the ATLAS<sup>3D</sup> sample (Paper III) together with the early spirals (Sa–Sb) and later spiral types (Sc–Irr) of the parent sample. There is a clear trend in the  $R_e$ – $L_K$  diagram as a function of galaxy morphology. To quantify this trend we fitted linear relations to the logarithmic coordinates assuming the same fractional errors for both axes and requiring  $\chi^2/\text{DOF} = 1$ . The fit was performed using the FITEXY routine which is based on the algorithm by Press et al. (1992) and

is part of the IDL Astronomy User’s Library<sup>6</sup> (Landsman 1993). The best-fitting power-law  $R_e$ – $L_K$  relations are

$$\log \left[ \frac{R_e(\text{FR})}{\text{kpc}} \right] = 0.53 + 0.44 \log \left[ \frac{L_K(\text{FR})}{10^{11} L_{\odot,K}} \right], \quad (1)$$

$$\log \left[ \frac{R_e(\text{Sa–Sb})}{\text{kpc}} \right] = 0.67 + 0.39 \log \left[ \frac{L_K(\text{Sa–Sb})}{10^{11} L_{\odot,K}} \right], \quad (2)$$

$$\log \left[ \frac{R_e(\text{Sc–Irr})}{\text{kpc}} \right] = 0.78 + 0.32 \log \left[ \frac{L_K(\text{Sc–Irr})}{10^{11} L_{\odot,K}} \right] \quad (3)$$

for fast rotators, Sa–Sb spirals and Sc or later spiral types, respectively. The slopes for the early and late spirals bracket the trend  $R_e \propto L_K^{0.35}$  found by Courteau et al. (2007). There is a clear known zone of avoidance at small sizes and large luminosities, which is also well defined in our parent sample and approximated above our luminosity limit by a double power law (cf. Lauer et al. 1995):

$$R_e = 2^{(\gamma-\beta)/\alpha} R_{e,b} \left( \frac{L_K}{L_{K,b}} \right)^\gamma \left[ 1 + \left( \frac{L_K}{L_{K,b}} \right)^\alpha \right]^{(\beta-\gamma)/\alpha}. \quad (4)$$

This equation defines a minimum effective radius  $R_{e,b} = 0.85$  kpc and a corresponding maximum effective surface brightness at a characteristic galaxy luminosity  $L_{K,b} = 2.5 \times 10^{10} L_{\odot,K}$  (cf. Graham & Worley 2008). The logarithmic power slope for  $L_K \ll L_{K,b}$  is  $\gamma = -0.15$ , while for  $L_K \gg L_{K,b}$  it is  $\beta = 0.75$ , so that for large luminosities  $R_e \propto L_K^{0.75}$ . A sharp transition between the two regimes is set by  $\alpha = 8$ .

Consistently with other larger local galaxy samples (van Dokkum et al. 2008; Trujillo et al. 2009; Taylor et al. 2010), we find no massive and superdense ( $L_K \gtrsim 10^{11} L_{\odot,K}$  and  $R_e \lesssim 2$  kpc) ETGs in our parent sample, contrary to what is found from photometry of ETGs at redshift  $z \gtrsim 1.5$  (e.g. Daddi et al. 2005; Trujillo et al. 2006; Cimatti et al. 2008; van Dokkum et al. 2008). Similar  $R_e$ – $L$  relations were derived by Shen et al. (2003) for early-type and late-type galaxies, defined as those having a Sersic (1968) index larger or smaller than  $n = 2.5$ , respectively. Their relation also showed a trend for late types to have larger sizes (by definition, due to the smaller  $n$ ) at given luminosity (or mass) and a more shallow  $R_e$ – $L$  relations, as we find using the morphological selection. A trend in the  $R_e$ – $M$  relation involving colours, with red-sequence galaxies having smaller sizes, can be seen in van Dokkum et al. (2008). While a trend involving age was presented by van der Wel et al. (2009) and Shankar & Bernardi (2009), and confirmed by Valentinuzzi et al. (2010), who find smaller sizes for older objects, at given stellar mass. All these trends are consistent with our finding using fast/slow rotators ETGs, in combination with traditional morphology of spiral galaxies (see also Bernardi et al. 2010), when one considers that later galaxy types tend to be more gas rich and have a younger stellar population. However here we interpret the observed trends as due to a variation in the bulge fraction, with bulges progressively increasing (by definition) from Sd–Sc to Sb–Sa and to fast rotators ETGs (see Paper VII). A detailed study of scaling relations in our sample will be presented in a subsequent paper.

<sup>6</sup> Available from <http://idlastro.gsfc.nasa.gov/>

### 3 THE ATLAS<sup>3D</sup> SAMPLE

#### 3.1 Morphological selection

We established that the ATLAS<sup>3D</sup> parent sample is essentially complete within the selection criteria and representative of the nearby galaxy population. We also verified that its luminosity function agrees with the one derived from much larger volumes of the Universe. The ATLAS<sup>3D</sup> survey however is focused on the study of the fossil record of galaxy formation as recorded in the structure of ETGs. The ATLAS<sup>3D</sup> sample is a subset of the parent sample, consisting of all the ETGs in that sample.

The distinction between red-sequence and blue-cloud galaxies is related, but different from the early type versus spiral morphological separation. E and S0 galaxies invariably lie on the red sequence, while late-type spirals are generally on the blue cloud. However large fractions of spirals populate the red sequence as well and overlap with ETGs (Strateva et al. 2001; Conselice 2006; van den Bergh 2007; Bernardi et al. 2010). An accurate morphology is easier to obtain for nearby galaxies and it is more robust than colour to dust and inclination effects. For this reasons a morphological classification is our preferred selection criterion.

To perform the morphological selection we considered using the morphological classification provided in available catalogues like the RC3 or its ongoing evolution HyperLeda. A problem with those classifications is the possible non-homogeneity of the classification process. Moreover the classification in those catalogues was performed using photometry in a single band, often from photographic plates. Given that for the majority of the galaxies in our parent sample excellent quality multiband photometry is available from the SDSS Data Release 7 (DR7; Abazajian et al. 2009), we decided to revisit the classification of the whole parent sample using the best available imaging.

The morphological classification of a given galaxy using multi-colour imaging may differ from the one obtained from photographic plates of the same object. None the less we tried as much as possible to be consistent with the currently accepted morphological criteria. We just need to separate the parent sample into two classes: ETGs and spirals. This makes our task much simpler and reproducible than a more detailed morphological classification into E, S0 and spiral subclasses Sa–Sd.

Since the introduction of the classic tuning-fork diagram by Hubble (1936), for the past half-century, essentially all authors have converged on a simple criterion to differentiate ETGs from spirals. The criterion, which defines the *revised* Hubble classification scheme, is outlined by Sandage (1961) in the Hubble Atlas and is based entirely on the presence of spiral arms (or dust lanes when seen edge-on): ‘the transition stages, S0 and SB0, are firmly established. In both sequences, the nebulae may be described as systems definitely later than E7 but showing no spiral structure’. This same criterion was adopted unchanged in the extension to the classification scheme by de Vaucouleurs (1959, 1963), which was applied to the widely used RC2 and RC3 catalogues (de Vaucouleurs, de Vaucouleurs & Corwin 1976; de Vaucouleurs et al. 1991) and HyperLeda (Paturel et al. 2003). Although other characteristics of galaxies change with morphological classification (e.g. the bulge/disc ratio), they are ignored in the separation between early types and spiral galaxies (see review by Sandage 1975). We adopted the same criterion here to select the ETGs belonging to the ATLAS<sup>3D</sup> sample from the parent sample.

Our morphological selection was done by visual inspection of the true-colour red–green–blue images (Lupton et al. 2004) provided

by the SDSS DR7 which are available for 82 per cent of the galaxies in the parent sample. For the remaining objects we used the *B*-band DSS2-blue images in the Online Digitized Sky Survey.<sup>7</sup> We revisited the classification for the galaxies without SDSS DR7 data after obtaining our own Isaac Newton Telescope (INT) imaging (Section 5.1) and this led to the removal of a couple of galaxies from the ETGs sample. At the end of our classification we compared the agreement between our separation into early types and spirals and the one provided by the *T* type given by HyperLeda, which defines as ETGs (E and S0) those having  $T \leq -0.5$ . We found agreement in 97 per cent of the cases, confirming the robustness and reproducibility of the morphological selection. The few disagreements with HyperLeda could all be easily explained by the high quality of the multicolour SDSS images, which allowed for a better detection of faint spiral structures. The ATLAS<sup>3D</sup> sample of 260 ETGs obtained from this selection is given in Table 3 and illustrated in Figs 5 and 6, together with the HyperLeda morphological classification as provided by their *T* type (E:  $T \leq -3.5$ ; S0:  $-3.5 < T \leq -0.5$ ; S0/a:  $-0.5 < T \leq 0.5$ ).

#### 3.2 Colour–magnitude diagram

The decision to select the ATLAS<sup>3D</sup> sample based on morphology instead of colour was based on (i) the broad similarity of the two criteria, (ii) the non-availability of reliable colours for the whole parent sample and (iii) the robustness of morphology, as opposed to colours, against dust extinction. Still, we expect the ATLAS<sup>3D</sup> sample to include mainly galaxies on the red sequence in a colour–magnitude diagram. This is verified in Fig. 7. The ATLAS<sup>3D</sup> sample of ETGs indeed defines a narrow colour–magnitude sequence approximated, in SDSS magnitudes, by

$$u - r = 2.53 - 0.097(M_r + 20). \quad (5)$$

As found by previous authors there is little scatter in the relation at the high-mass end, while at the lower mass end some galaxies appear to be still in transition between the blue and red sequence (Strateva et al. 2001; Conselice 2006; van den Bergh 2007; Bernardi et al. 2010). The 31 ETGs with SDSS colour and defined as slow rotators in Paper III all lie close to the red sequence with an rms scatter of 0.13 mag from the best-fitting relation. All the deviants ETGs are classified as fast rotators in Paper III. The nature of these objects will be investigated in detail in subsequent papers of this series. Spiral galaxies span the full region of the diagram, both on the red sequence and the blue clouds, as found by previous studies.

### 4 SAURON DATA FOR THE ATLAS<sup>3D</sup> SURVEY

#### 4.1 Observing strategy

The main aim of the SAURON (Bacon et al. 2001) observations of the ATLAS<sup>3D</sup> sample is to obtain global galaxy quantities like the specific stellar angular momentum  $\lambda_R$ , the  $(V/\sigma, \epsilon)$  the global kinematical misalignment, the luminosity-weighted second moment  $\sigma_e$ , the stellar and total mass-to-light ratio, the mean stellar population and the ionized gas emission. To be representative of the galaxies as a whole, these quantities need to be measured at least within one projected half-light radius  $R_e$ . Moreover for a given observed area, more accurate values of the kinematical quantities are obtained when the quantities are measured within ellipses instead of

<sup>7</sup> <http://archive.eso.org/dss>

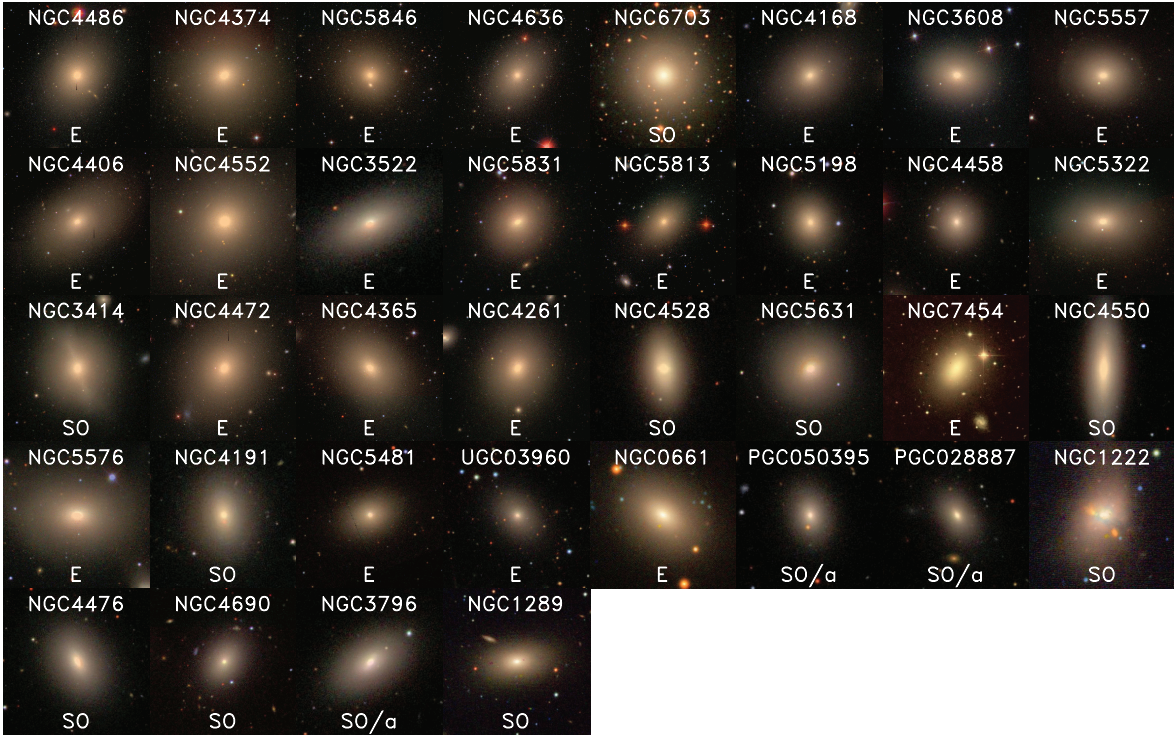


**Figure 5.** Morphology of slow-rotators ETGs sorted by increasing  $\lambda_R$ . Postage stamps of the SDSS DR7 and INT red–green–blue composite images of slow rotators in the ATLAS<sup>3D</sup> sample. The image of each galaxy was scaled so that the plot side is equal to  $10R_e$ , where  $R_e$  is the projected half-light radius given in Table 3. From left to right and from top to bottom the panels are sorted according to their specific stellar angular momentum, as measured by the parameter  $\lambda_R$  given in Paper III. The galaxy name is given at the top of each panel and the morphological classification from HyperLeda at the bottom. At this scale slow-rotator ETGs appear generally featureless except for the synchrotron jet in NGC 4486 and obvious signs of interactions in NGC 1222, NGC 3414 and NGC 5557. The only significant flat galaxy in this class is NGC 4550, while two other galaxies NGC 3796 and NGC 4528 show evidence of bar perturbations, which is typically associated to stellar discs. All these three objects contain counter-rotating stellar discs (Paper II). (This figure is better appreciated on a computer screen rather than on printed paper.) A version of Figs 5 and 6 sorted by name is available at <http://purl.org/atlas3d>.

circles, with ellipticity given by the galaxy photometry and the position angle defined by the stellar kinematics (see appendix B of Cappellari et al. 2007). In addition, when galaxies are barred, the SAURON survey has shown that the kinematics are generally still aligned with the position angle of the galaxy photometry at large radii  $PA_{\text{phot}}$  (Krajnović et al. 2008), which defines the position of the line-of-nodes of the disc. These requirements, which derive from our experience with the SAURON survey (de Zeeuw et al. 2002), lead to the following optimized observing strategy, which we systematically applied for the SAURON observation of the ATLAS<sup>3D</sup> sample.

(i) When  $R_e \leq 30$  arcsec take a single SAURON field and orient the SAURON major axis with the large radii  $PA_{\text{phot}}$ .

(ii) When  $R_e > 30$  arcsec then we take a mosaic of two SAURON fields. Given the size of the SAURON field of  $33 \times 41$  arcsec<sup>2</sup>, the criterion of maximizing the area of the largest isophote, of axial ratio  $q'$ , enclosed within the observed field-of-view, becomes

(a) if  $q' < 0.55$  the SAURON long axis is aligned with  $PA_{\text{phot}}$  and the mosaic is made by matching the two SAURON pointings along the short side;

(b) if  $q' \geq 0.55$  the SAURON short axis is aligned with  $PA_{\text{phot}}$  and the mosaic is made by matching the two SAURON pointings along the long side.

At the time of the SAURON observations the only photometry available to us for the whole sample was from 2MASS. We adopted the  $R_e$  provided by the 2MASS XSC, which is determined via

growth curves within elliptical apertures. Specifically, in terms of the XSC catalogs parameters, we defined

$$R_e^{2\text{MASS}} = \text{MEDIAN}(j_{r,\text{eff}}, h_{r,\text{eff}}, k_{r,\text{eff}}) \sqrt{k_{\text{ba}}}, \quad (6)$$

as the median of the three 2MASS values in the  $J$ ,  $H$  and  $K_s$  band, where the factor  $\sqrt{k_{\text{ba}}}$  takes into account the fact that the 2MASS values are the semimajor axes of the ellipses enclosing half of the galaxy light and we want the radius of the circle with the same area. This  $R_e^{2\text{MASS}}$  was compared to the  $R_e^{\text{RC3}}$  provided by the RC3 catalogue and measured via growth curves within circular apertures. The two values correlate well, with an observed rms scatter of 0.12 dex in  $R_e$ , which implies an error of about 22 per cent in each  $R_e$  determination (assuming they have similar errors). However there is a general offset by a factor  $R_e^{\text{RC3}} \approx 1.7 R_e^{2\text{MASS}}$  between the two determinations (Fig. 8). The rms scatter in the  $R_e^{\text{RC3}} - R_e^{2\text{MASS}}$  correlation is close to the one (0.11 dex) we obtain when comparing  $R_e^{\text{RC3}}$  to 46 values determined using growth curves in the  $I$  band for the SAURON survey (Cappellari et al. 2006; Kuntschner et al. 2006). In that case however the offset in the values is negligible (factor 0.95). We conclude that the 2MASS  $R_e$  determinations have comparable accuracy to the RC3 and SAURON determination, when they are increased by a factor of 1.7 to account for the differences in the observed photometric band and in the depth of the photometry data. All three values are consistent with having a similar error of  $\approx 22$  per cent in  $R_e$ . This rather large error is consistent with the findings of Chen et al. (2010) from another extensive comparison of  $R_e$  values. To further improve the accuracy we adopted



**Figure 6.** Same as in Fig. 5 for the fast-rotators ETGs in the ATLAS<sup>3D</sup> sample, sorted by increasing  $\lambda_R$ . The first panel contains mostly round objects. Many of them are barred (Paper II), nearly face-on, S0 galaxies and often contain stellar rings (e.g. NGC 4608), while others appears face-on from the geometry of their dust. This suggests that the round shape and low  $\lambda_R$  of these objects is not intrinsic, but due to their low inclination ( $i = 90^\circ$  being edge on). On the contrary the last panel is dominated by nearly edge-on discs, which explains their high  $\lambda_R$ .



Figure 6 – *Continued*



Figure 6 – Continued

$R_e = (1.7 R_e^{2\text{MASS}} + R_e^{\text{RC3}})/2$  for the 412/871 galaxies with both 2MASS and RC3 determinations and  $R_e = 1.7 R_e^{2\text{MASS}}$  when only 2MASS was available. The values of  $R_e$  for the full parent sample, divided into ETGs and spirals, are given in Tables 3 and 4.

#### 4.2 Integral field spectroscopic observations

The SAURON integral field spectrograph was first mounted at the WHT at the Observatory of El Roque des Los Muchachos on La Palma in 1999. It has been used extensively in particular in the course of the SAURON survey, but also in separate smaller efforts (e.g. Bower et al. 2004; Allard, Peletier & Knapen 2005; Dumas et al. 2007; Weijmans et al. 2010). Given that the ATLAS<sup>3D</sup> selection criteria are by design very similar to the ones in the SAURON survey, a total of 64 ETGs had been observed before the beginning of the ATLAS<sup>3D</sup> observing campaign. 49 ETGs were part of the main survey (de Zeeuw et al. 2002), out of which 47 were presented in the subsample of ETGs (Emsellem et al. 2004) and two in the early-spirals subsample (Falcón-Barroso et al. 2006). 14 ‘special’ ETGs within the ATLAS<sup>3D</sup> volume had been observed with SAURON in the course of other projects (table 3 of Cappellari et al. 2007). All these galaxies were observed before the volume phase holographic (VPH) grating came into use and were taken with an exposure time of 2 h on source, in some cases with multiple spatial pointings to cover galaxies to roughly one effective (projected half-light  $R_e$ ) radius. All the observations were obtained in the low spatial resolution mode in which the instrument has a field-of-view of  $33 \times 41 \text{ arcsec}^2$  sampled with  $0.94 \text{ arcsec}^2$  lenslets and with a

spectral resolution of  $4.2 \text{ \AA}$  full width at half-maximum (FWHM;  $\sigma_{\text{instr}} = 105 \text{ km s}^{-1}$ ), covering the wavelength range  $4800\text{--}5380 \text{ \AA}$ .

To observe the additional 196 galaxies we were allocated 38 observing nights comprising four observing runs spread over three consecutive semesters as part of a long-term project at the WHT (Table 5). The time allocation was split equally between Dutch and UK time. We had excellent weather with just 16 per cent of nights lost due to clouds, compared to a normal average for the period of around 30 per cent. This fact, combined with an efficient observing strategy allowed us to complete all observations of the ATLAS<sup>3D</sup> sample galaxies in the allocated time.

The optimal scheduling of the observations of the 196 galaxies, in some cases using multiple spatial pointings, was performed with a dedicated IDL script which gave higher priority to the intrinsically brightest galaxies, took into account the galaxy coordinates, the need for multiple pointings, the dates of the four observing runs and the moon position and phase. The script could be easily re-run to modify the scheduling to account for time lost due to bad weather. The observations were performed with the VPH grating, which provides a resolution of  $3.9 \text{ \AA}$  FWHM ( $\sigma_{\text{instr}} = 98 \text{ km s}^{-1}$ ), about 7 per cent better than for the SAURON survey. The adopted on-source exposure time was 1 h, split into two equal 30-min exposure dithered by a couple of arcseconds.

#### 4.3 Data reduction and stellar kinematics extraction

The SAURON data reduction followed standard procedures and used the dedicated xSAURON software developed at Centre de

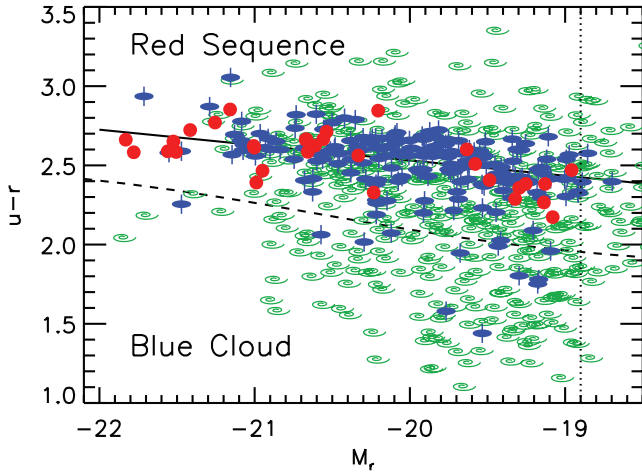


**Figure 7.**  $u - r$  versus  $M_r$  colour–magnitude diagram for the morphologically selected ATLAS<sup>3D</sup> parent sample with SDSS photometry. The blue ellipses with axis are fast-rotator ETGs, the red filled circles are slow-rotators ETGs, while the green spirals are spiral galaxies. The dashed line indicates the separation between red sequence and blue cloud established by Baldry et al. (2004, 2006), from a sample of 151 642 galaxies. The vertical dotted line indicates our approximate survey completeness limit in  $r$  band  $M_r \lesssim -18.9$  mag. The solid line is a linear robust fit to the ETGs only, minimizing the sum of the absolute residuals.

Recherche Astronomique de Lyon (CRAL) and was already described in Bacon et al. (2001) and Emsellem et al. (2004). However some details of our approach have been improved after the original publication of the data. For this reason we re-extracted all the stellar kinematics using the improved and completely homogeneous approach for the entire ATLAS<sup>3D</sup> data set. We describe here the minor differences with respect to what was published before.

The data were spatially binned with the adaptive Voronoi method<sup>8</sup> of Cappellari & Copin (2003), which optimally solves the problem of preserving the maximum spatial resolution of two-dimensional data, given a constraint on the minimum signal-to-noise ratio (S/N). We adopted a target S/N = 40 for all the data used in the ATLAS<sup>3D</sup> survey, including the previous SAURON observations, which were re-extracted adopting for consistency this lower S/N instead of the S/N = 60 as originally published in Emsellem et al. (2004).

The stellar kinematics were extracted with the penalized pixel-fitting (pPXF) software<sup>8</sup> (Cappellari & Emsellem 2004), which simultaneously fits the stellar kinematics and the optimal linear combination of spectral templates to the observed spectrum, using a maximum-likelihood approach to suppress noisy solutions. The line-of-sight velocity distribution (LOSVD) is described via the Gauss–Hermite parametrization up to  $h_3$ – $h_4$  (Gerhard 1993; van der Marel & Franx 1993). We employed as stellar template an optimal linear combination of stars from the MILES library<sup>9</sup> (Sánchez-Blázquez et al. 2006), which was separately determined for every galaxy. We did not allow the template to change in every bin to eliminate small artefacts in the kinematics due to imperfections in the velocity alignment of the MILES stars. A resolution of 2.56 Å FWHM was adopted for the stars. We adjusted the penalty in pPXF to a value  $\lambda = 0.5$ , optimized for the adopted S/N. Following the pPXF documentation we determined the optimal  $\lambda$  by requiring the maximum bias in the Gauss–Hermite parameters  $h_3$  and  $h_4$  to

<sup>8</sup> Available from <http://purl.org/cappellari/idl>

<sup>9</sup> Available from <http://miles.iac.es/>

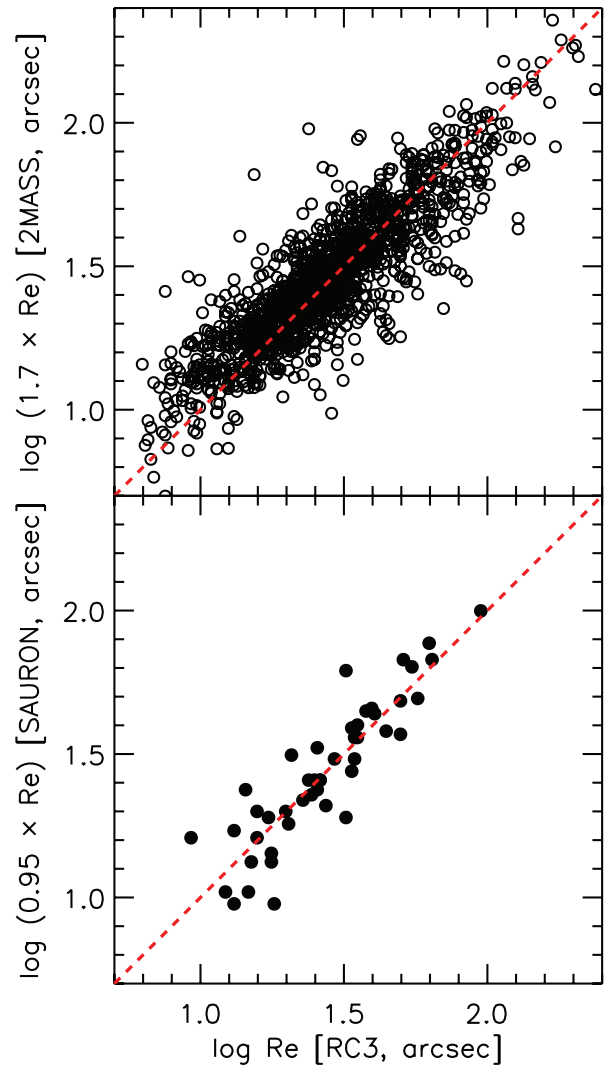


**Figure 8.** Testing the accuracy of  $R_e$  determinations. Top panel: comparison between 1353 values of  $R_e$  given by RC3 and the ones given by 2MASS (computed as described in the text), scaled by the best-fitting factor of 1.7. Bottom panel: same as in the top panel for the RC3  $R_e$  and the ones for 46 ETGs of the SAURON survey. Once corrected for systematic differences, all three  $R_e$  determinations are consistent with a similar error of  $\approx 22$  per cent.

**Table 5.** SAURON observing runs for the ATLAS<sup>3D</sup> sample.

Run	Dates	Clear
1	2007 April 10–23	12/14
2	2007 August 13–15	3/3
3	2008 January 9–15	6/7
4	2008 February 27–March 11	11/14

be equal to  $\text{rms}/3$ , where the rms is the scatter of the measurements obtained from a Monte Carlo simulations with the adopted S/N = 40 and a well resolved stellar dispersion  $\sigma \gtrsim 180 \text{ km s}^{-1}$  (Fig. 9). In a handful of cases we could not reach the required S/N without employing excessively large Voronoi bins. In those cases we further reduced the target S/N. For those galaxies we correspondingly adapted the penalty in pPXF according to the empirical relation of Fig. 10. For usage in cases where we need to approximate the stellar

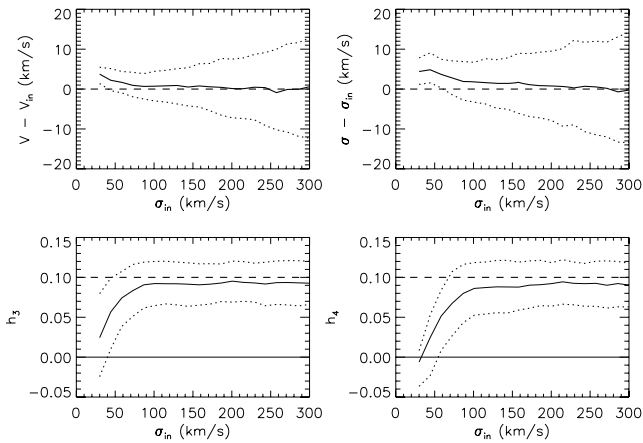


**Figure 9.** Testing penalization in ppxf. We simulated spectra with the S/N = 40 of our data and an LOSVD with  $h_3 = 0.1$ ,  $h_4 = 0.1$  and  $\sigma$  in the range between 30 and 300 km s<sup>-1</sup>. We extracted the kinematics with ppxf and a penalty  $\lambda = 0.5$ . The lines in the top two panels show the 50th (median, solid line), 16th and 84th percentiles (1 $\sigma$  errors, dotted lines) of the differences between the measured values and the input values of the mean velocity  $V_{in}$  and the velocity dispersion  $\sigma_{in}$ . The bottom panels show the same lines for the recovered values of  $h_3$  and  $h_4$ , compared to the input values (dashed line). The  $h_3$  and  $h_4$  parameters can only be recovered when  $\sigma_{in} \gtrsim 100$  km s<sup>-1</sup>. Typical statistical errors in the kinematics parameter for  $\sigma_{in} \approx 200$  km s<sup>-1</sup> are 6 km s<sup>-1</sup>, 7 km s<sup>-1</sup>, 0.03 and 0.03 for  $V$ ,  $\sigma$ ,  $h_3$  and  $h_4$ , respectively.

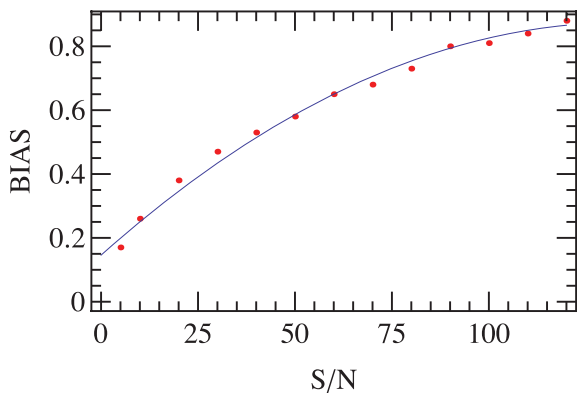


**Figure 10.** Relation between the S/N of the SAURON spectrum and the optimal penalty parameter  $\lambda$  (keyword BIAS) in ppxf. The solid line is the polynomial  $\text{BIAS} = 0.15 + 0.0107 S/N - 0.00004 (S/N)^2$ .

velocity second moments and not the full LOSVD – e.g. to fit models based on the Jeans (1922) equations or measure  $\lambda_R$  or  $V/\sigma$  – we separately extracted the kinematics assuming a simple Gaussian LOSVD. In that case the ppxf penalty is ignored. In all cases the errors on the kinematics were determined via bootstrapping (Efron & Tibshirani 1993), by randomly resampling the ppxf fit residuals of the best fit and repeating the kinematic fit for 100 realizations, with a zero penalty (see section 3.4 of Cappellari & Emsellem 2004). The homogeneous set of integral field SAURON kinematics introduced in this paper, together with the stellar population parameters, the characteristics of the ionized gas and the entire data cubes for the full ATLAS<sup>3D</sup> sample will be made available via the project web page<sup>10</sup> at the end of our project.

As discussed in detail in Cappellari & Emsellem (2004) and illustrated in Fig. 9, the SAURON spectroscopic data allow the

extraction of the full stellar LOSVD, including the Gauss–Hermite parameters, only for observed velocity dispersions  $\sigma \gtrsim 120$  km s<sup>-1</sup>. Below this value the  $h_3$  and  $h_4$  start becoming unconstrained by the data, due to the spectral undersampling and for this reason the ppxf method automatically and gradually penalizes them towards zero to keep the noise on the mean velocity  $V$  and velocity dispersion  $\sigma$  under control. As the minimum S/N of our data is defined by our Voronoi binning criterion, the level of bias depends only on  $\sigma$  as illustrated in the Monte Carlo simulation of Fig. 9. This effect is also illustrated for ATLAS<sup>3D</sup> data in Fig. 11, for a small set of galaxies with a range of luminosity-weighted  $\sigma_e$  within  $1R_e$  (defined as in Cappellari et al. 2006). The figure shows the range of data quality for the stellar kinematical data for the ATLAS<sup>3D</sup> survey. At high  $\sigma_e$  the data have a quality which is comparable to the one for the SAURON survey presented in Emsellem et al. (2004). The shorter exposure time of the ATLAS<sup>3D</sup> survey is in part compensated by the use of the VPH grating and in part by the adoption of larger Voronoi bins. However at  $\sigma_e \lesssim 120$  km s<sup>-1</sup> there is not enough information in the data to constrain  $h_3$  and  $h_4$ . Contrary to the SAURON survey the volume-limited ATLAS<sup>3D</sup> survey is dominated by the more common low-luminosity galaxies, which also tend to have low dispersion. In practice we find that  $\approx 40$  per cent of the galaxies in the sample have  $\sigma_e \lesssim 120$  km s<sup>-1</sup> and for those objects we can only recover reliable  $V$  and  $\sigma$  values. Although the kinematics are not sufficient to constrain general dynamical models for the full sample, they still provide very reliable global values of specific angular momenta and galaxy masses for all galaxies (e.g. Cappellari et al. 2010).

We also used the SAURON stellar kinematic to measure extremely robust heliocentric recession velocities  $V_{\text{hel}}$  for all galaxies in the sample. Repeated determinations indicate a 1 $\sigma$  accuracy  $\Delta V_{\text{hel}} \approx 5$  km s<sup>-1</sup>. The values were derived from the integral field stellar kinematics by finding the value which needs to be subtracted from the observed velocity field to best fit a bi-antisymmetric version of the velocity field.<sup>11</sup> This technique does not suffer from the uncertainties due to the slit centring, which affects spectroscopic surveys, or from the possibility of the gas not being associated to the galaxy, which affects H I determinations. The observed velocities were converted into velocities  $V_{\text{hel}}$  relative to the barycentre of the Solar system via the IDL routine BARYVEL, which implements the algorithm by Stumpff (1980) and is part of the IDL Astronomy User’s Library (Landsman 1993). The measured  $V_{\text{hel}}$  values are given in Table 3.

## 5 ADDITIONAL ATLAS<sup>3D</sup> DATA AND SIMULATIONS

### 5.1 H I, CO and optical observations

Apart from the SAURON integral field spectroscopic observations presented in detail in Section 4, the ATLAS<sup>3D</sup> survey includes other multiwavelength observations obtained with different instruments and facilities. These data sets will be presented in subsequent papers, however, a summary of the main ones is presented in Table 6, and more information are given below.

(i) *H I interferometry.* We have observed the H I properties of all galaxies in the ATLAS<sup>3D</sup> sample above  $\delta = 10^\circ$  (due to the

<sup>11</sup> This was performed with the IDL routine FIT\_KINEMATICS\_PA described in appendix C of Krajnović et al. (2006) and available at <http://purl.org/cappellari/idl>

<sup>10</sup> <http://purl.org/atlas3d>

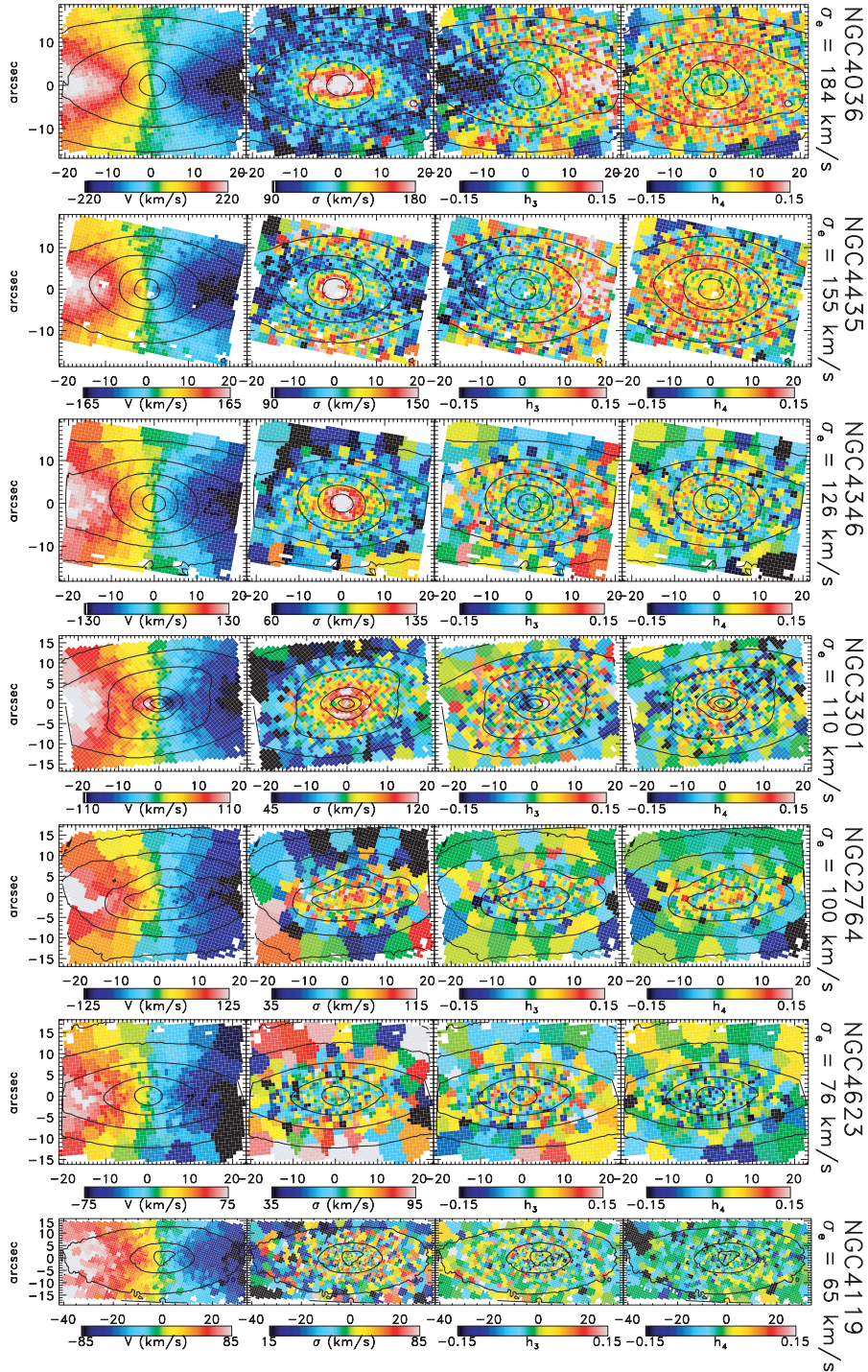


**Figure 11.** Quality of the SAURON stellar kinematics in the ATLAS<sup>3D</sup> survey. Each column from left to right shows the Voronoi binned kinematic moments extracted via ppxf from the SAURON data: mean velocity,  $V$ , velocity dispersion,  $\sigma$ , and higher Gauss–Hermite moments,  $h_3$  and  $h_4$ . From top to bottom the data for seven newly observed fast rotators in the ATLAS<sup>3D</sup> sample are sorted according to the luminosity-weighted dispersion  $\sigma_e$  within  $1R_e$ . Below  $\sigma_e \lesssim 120 \text{ km s}^{-1}$  the data have insufficient information to constrain the full LOSVD and the Gauss–Hermite moments are automatically and gradually suppressed by ppxf towards zero to reduce the noise in  $V$  and  $\sigma$ , which can still be reliably recovered. About 40 per cent of the galaxies in the sample have  $\sigma_e \lesssim 120 \text{ km s}^{-1}$ .

telescope latitude). This subsample includes 170 galaxies – 43 inside and 127 outside the Virgo cluster. We observed all galaxies outside Virgo, and galaxies inside Virgo detected by the Alfafa survey (Giovanelli et al. 2005), with the Westerbork Synthesis Radio Telescope (WSRT). Some of the galaxies were observed with the WSRT as part of previous studies (Morganti et al. 2006; Józsa et al.

2009; Oosterloo et al. 2010). The integration time for all galaxies observed with the WSRT is 12 h, providing H I cubes at a resolution of  $\sim 30 \text{ arcsec}$  and  $16 \text{ km s}^{-1}$  over a field of view of  $\sim 1 \text{ deg}^2$  and a velocity range of  $\sim 4000 \text{ km s}^{-1}$ . We detect H I gas down to a column density of a few times  $10^{19} \text{ cm}^{-2}$ . The upper limits on  $M(\text{H I})$  derived from these data ranges between  $10^6$  and a few times

**Table 6.** Multiwavelength ATLAS<sup>3D</sup> data.

Instrument	Tracer/band/res.	Number of objects	Selection	Reference	Time allocation
WSRT	H I @ 21 cm	170	$\delta > 10^\circ$	Serra et al. (in preparation)	1212 h
IRAM 30-m	<sup>12</sup> CO $J = 1-0$ and $2-1$	259	All	Paper IV	211 h
CARMA	<sup>12</sup> CO $J = 1-0$	32	$f > 19 \text{ Jy km s}^{-1}$	Alatalo et al. (in preparation)	467 h
INT + SDSS	$u, g, r, i, z$	35 + 225	All	Scott et al. (in preparation) + Abazajian et al. (2009)	5 n
SAURON	480–538 nm; $R = 1300$	260	All	This paper	38 n

$10^7 M_\odot$  depending on galaxy distance. This is typically about five times lower than upper limits derived from Alfalfa spectra. These observations and a discussion of the H I properties will be presented in Serra et al. (in preparation). Interesting objects, like extended discs, have been followed-up for deeper H I observations.

(ii) *CO single dish.* All of the ATLAS<sup>3D</sup> galaxies have been searched for <sup>12</sup>CO  $J = 1-0$  and  $2-1$  emission with the IRAM 30-m telescope, including 204 new observations with the remainder collected from the recent literature. The data consist of a single pointing at the galaxy centre, covering a bandwidth of  $1300 \text{ km s}^{-1}$  centred on the optical velocity. The rms noise levels of the  $1-0$  spectra are  $3 \text{ mK } (T_A^*)$  or better after binning to  $31 \text{ km s}^{-1}$  channels, so that the  $3\sigma$  upper limit for a sum over a  $300 \text{ km s}^{-1}$  linewidth corresponds to a  $\text{H}_2$  mass  $\sim 1 \times 10^7 M_\odot$  for the most nearby sample members and  $\sim 1 \times 10^8 M_\odot$  for the most distant members. A detailed description of the observations and the corresponding measurements is presented in Paper IV.

(iii) *CO interferometry.* The brighter CO detections have been, observed in the  $1-0$  line with the BIMA, Plateau de Bure, and CARMA millimeter interferometers in order to map the distribution and kinematics of the molecular gas. These observations are designed to provide the molecular surface densities and angular momenta for 80 per cent of all of the molecular gas found in the ATLAS<sup>3D</sup> sample, typically at resolutions of 5 arcsec. Some additional data at higher and lower resolutions are obtained as necessary to probe the structure of the gas and recover the bulk of the emission detected in the single dish data. On-source integration times range from 4 to 20 h and are also adjusted as necessary for high-quality detections. A detailed description of the observations and the corresponding measurements is presented in Alatalo et al. (in preparation).

(iv) *INT optical imaging.* Observations with the Wide-Field Camera (WFC) at the 2.5-m INT were carried out to obtain  $u, g, r, i$  and  $z$ -band imaging for galaxies not observed by the SDSS. Images were taken through the five filters for 55 galaxies from the ATLAS<sup>3D</sup> sample. Integration times were typically 60 to 160 s reaching sensitivities comparable or deeper than the SDSS. Galaxies already observed by SDSS were observed in the runs as a cross-check in general and to bring the INT imaging on to the same photometric system as SDSS in particular. The images have been reduced and calibrated using the Astro-WISE system (Valentijn et al. 2007). A detailed description of the observations and the corresponding measurements is presented in Scott et al. (in preparation).

(v) *Targeted follow-ups.* We are also obtaining data for targeted subsets of the sample: deep optical images of ATLAS<sup>3D</sup> galaxies were obtained with the MegaCam camera installed on the Canada–France–Hawaii Telescope. This imaging part of the project aims to reach surface brightness limits as low as  $28.5 \text{ mag arcsec}^{-2}$  in the  $g$  band. Reaching such values allows to disclose very faint, diffuse structures in the outskirts of the ETGs, such as shells and tidal tails, that tell about their past mass accretion history. We have also started an observing campaign to obtain stellar kinematics and

absorption line strengths out to large radii ( $3-5 R_e$ ) with integral field units (IFUs; e.g. SAURON, VIRUS-P) for a number of ATLAS<sup>3D</sup> galaxies. Following the methods outlined in Weijmans et al. (2009) we will construct dynamical models to trace the halo mass profiles. We primarily target galaxies that have been detected in H I to have a regularly rotating disc and ring, so that the H I kinematics can be added to the dynamical modelling.

## 5.2 Numerical simulations

The ATLAS<sup>3D</sup> project includes a theoretical effort to interpret the observations using models of galaxy formation. We are attacking the problem via three parallel approaches as described below.

(i) *Binary mergers.* An extensive set of ‘idealized’ (i.e. without the cosmological context) numerical simulations is being conducted. These simulations have been made at an unmatched resolution (softening length of 58 pc and a total number of particles of  $1.2 \times 10^7$ ) with the goal to better understand the role of mergers in the formation and evolution of galaxies of the red sequence and to understand in details the physical processes involved during a merger (e.g. the formation of the kinematically decoupled components, the energy and angular momentum exchanges). These simulations are also a powerful tool to perform direct comparisons with observations such as e.g. the morphology via the ellipticity, the kinematics via  $\lambda_R$ , the redistribution of the gas at large scales, the metallicity gradients and the  $\text{Mg } b-V_{\text{esc}}$  relation (Davies, Sadler & Peletier 1993; Scott et al. 2009). The detailed description of the simulations and their associated results are presented in Bois et al. (2010) and Paper VI. Other idealized simulations of ATLAS<sup>3D</sup> galaxies are performed with the RAMSES high-resolution grid-based hydrodynamical code (Teyssier 2002). Following the technique developed in Bournaud et al. (2010), we model the dynamics of atomic and molecular gas discs in ETGs with parsec-scale resolution, based on accurate mass models extracted from the ATLAS<sup>3D</sup> data. These models aim at understanding the dynamics, stability and star formation activity of the interstellar medium in ETGs.

(ii) *Semi-analytic modelling.* In a second strand of simulations we address the formation of elliptical galaxies within a large-scale cosmological setting using a semi-analytic modelling (SAM) approach. Using the knowledge gained from idealized high-resolution simulations of mergers and the formation of a limited number of cosmologically simulated ETGs we test formation scenarios within our SAM making full use of the completeness of the ATLAS<sup>3D</sup> sample. The SAM we use is an extension of earlier work by Khochfar & Burkert (2005) and Khochfar & Silk (2006). Within the SAM we follow the individual history of a large statistical sample of galaxies to the present day, taking into account their merging history and physical processes related to e.g. gas cooling or star formation. In addition the SAM is used to make predictions on the evolution of these classes of ETGs that can be tested with future observations (Paper VIII).

(iii) *Cosmological simulations.* We will also make use of high-resolution simulations of individual galaxies in a full cosmological context (i.e. Naab et al. 2007; Naab, Johansson & Ostriker 2009) to investigate the physical processes setting the present day kinematical properties of ETGs. We will use a new sample of simulations (Oser et al. 2010) covering the full mass range of the ATLAS<sup>3D</sup> galaxies. From these simulated galaxies we will construct two-dimensional kinematical maps (Jesseit et al. 2007) to compare directly to the ATLAS<sup>3D</sup> observations. The use of cosmological simulations is advantageous as we can link the present day properties to the evolutionary history embedded in the favoured cosmology. We will also be able to investigate the influence of the merging history, dark matter and various feedback mechanisms on kinematic properties and the stellar populations.

## 6 SUMMARY

We described the motivation and goals of the ATLAS<sup>3D</sup> project, which aims at constraining models of galaxy formation by obtaining two-dimensional observations of the distribution and kinematics of the atomic (H I), molecular (CO) and ionized gas, together with the stellar population and kinematics, for a volume-limited nearly mass-selected ( $K_s$  band) sample of ETGs.

We defined the selection criteria for the volume-limited ( $1.16 \times 10^5 \text{ Mpc}^3$ ) parent sample of 871 galaxies with  $D < 42 \text{ Mpc}$  and  $M_K < -21.5 \text{ mag}$ , satisfying our observability criteria, and investigated possible selection biases, especially due to redshift incompleteness. We found that incompleteness cannot amount to more than a couple of per cent, making the sample essentially complete and representative of the nearby population. We additionally tested the representativeness of the sample by comparing its  $K_s$ -band luminosity function with the one derived from a much larger sample (Bell et al. 2003) and found a very good agreement. We described the morphological selection used to extract the 260 ETGs of the ATLAS<sup>3D</sup> sample from the parent sample and showed that the ETGs define a narrow red sequence, on a colour–magnitude diagram, with few objects in transition from the blue cloud. We presented the size–luminosity relation for the ATLAS<sup>3D</sup> sample and the full parent sample to illustrate the general characteristic of our galaxies.

We described the strategy for the SAURON integral field observations, the data reduction, the extraction of the stellar kinematics and their typical errors. We gave an overview of the additional data set already available for our sample, which include interferometric observations of the atomic gas as traced by H I, single dish and interferometric observations of molecular gas as traced by the CO lines and multiband optical photometry. We summarized the ongoing semi-analytic modelling and the cosmological and binary-merger  $N$ -body simulations we are performing to interpret our observations.

This is the first paper of a series devoted to our understanding of the formation of ETGs. Key additional elements are provided by the kinematics, ages and chemical composition of the stars in the galaxies, the presence of cold atomic or molecular gas, the photometric profiles and the dynamical masses, as a function of environment. The observations for the ATLAS<sup>3D</sup> sample will be compared against the model predictions to test formation scenarios and to tune the model parameter. This will be the topic of future papers of this series. The ATLAS<sup>3D</sup> project aims to constitute a zero redshift baseline, against which one can investigate the evolution of galaxy global parameters with redshift, to trace galaxy evolution back in time. Future studies should extend this effort to more dense environment than can be explored in the nearby universe, and to

increasingly higher redshifts to explore the time evolution of the structure of ETGs.

## ACKNOWLEDGMENTS

We thank to the anonymous referee for a useful report. MC acknowledges support from a STFC Advanced Fellowship PP/D005574/1 and a Royal Society University Research Fellowship. This work was supported by the rolling grants ‘Astrophysics at Oxford’ PP/E001114/1 and ST/H002456/1 and visitors grants PPA/V/S/2002/00553, PP/E001564/1 and ST/H504862/1 from the UK Research Councils. RLD acknowledges travel and computer grants from Christ Church, Oxford and support from the Royal Society in the form of a Wolfson Merit Award 502011.K502/jd. RLD also acknowledges the support of the ESO Visitor Programme that funded a 3-month stay in 2010. SK acknowledges support from the Royal Society Joint Projects Grant JP0869822. RMM is supported by the Gemini Observatory, which is operated by the Association of Universities for Research in Astronomy, Inc., on behalf of the international Gemini partnership of Argentina, Australia, Brazil, Canada, Chile, the United Kingdom and the United States of America. TN and MBo acknowledge support from the DFG Cluster of Excellence ‘Origin and Structure of the Universe’. MS acknowledges support from a STFC Advanced Fellowship ST/F009186/1. NS and TAD acknowledge support from an STFC studentship. The authors acknowledge financial support from ESO. We acknowledge the usage in `ppxf` of the `mpfit` routine by Markwardt (2009). The SAURON observations were obtained at the WHT, operated by the Isaac Newton Group in the Spanish Observatorio del Roque de los Muchachos of the Instituto de Astrofísica de Canarias. We are grateful to the ING staff for their excellent support and creativity in quickly solving technical problem during the SAURON runs. We are grateful to Jesús Falcon-Barroso for useful discussions and help with the observations. MC is grateful to the NED staff for prompt support. This research has made use of the NASA/IPAC Extragalactic Database (NED) which is operated by the Jet Propulsion Laboratory, California Institute of Technology, under contract with the National Aeronautics and Space Administration. We acknowledge the usage of the HyperLeda data base (<http://leda.univ-lyon1.fr>). Funding for the SDSS and SDSS-II was provided by the Alfred P. Sloan Foundation, the Participating Institutions, the National Science Foundation, the US Department of Energy, the National Aeronautics and Space Administration, the Japanese Monbukagakusho, the Max Planck Society and the Higher Education Funding Council for England. The SDSS was managed by the Astrophysical Research Consortium for the Participating Institutions. This publication makes use of data products from the Two Micron All Sky Survey, which is a joint project of the University of Massachusetts and the Infrared Processing and Analysis Center/California Institute of Technology, funded by the National Aeronautics and Space Administration and the National Science Foundation.

## REFERENCES

- Abazajian K. N. et al., 2009, *ApJS*, 182, 543
- Allard E. L., Peletier R. F., Knapen J. H., 2005, *ApJ*, 633, L25
- Bacon R. et al., 2001, *MNRAS*, 326, 23
- Baldry I. K., Glazebrook K., Brinkmann J., Ivezić Ž., Lupton R. H., Nichol R. C., Szalay A. S., 2004, *ApJ*, 600, 681
- Baldry I. K., Balogh M. L., Bower R. G., Glazebrook K., Nichol R. C., Bamford S. P., Budavari T., 2006, *MNRAS*, 373, 469
- Barnes J. E., 1992, *ApJ*, 393, 484

- Bell E. F., de Jong R. S., 2001, *ApJ*, 550, 212
- Bell E. F. et al., 2003, *ApJS*, 149, 289
- Bell E. F. et al., 2004, *ApJ*, 608, 752
- Bender R., Surma P., Doebereiner S., Moellenhoff C., Madejsky R., 1989, *A&A*, 217, 35
- Bender R., Burstein D., Faber S. M., 1992, *ApJ*, 399, 462
- Bernardi M., Shankar F., Hyde J. B., Mei S., Marulli F., Sheth R. K., 2010, *MNRAS*, 404, 2087
- Binney J., 1978, *MNRAS*, 183, 501
- Blakeslee J. P. et al., 2009, *ApJ*, 694, 556
- Blakeslee J. P. et al., 2010, *ApJ*, 724, 657
- Bois M. et al., 2010, *MNRAS*, 406, 2405
- Bois M. et al., 2011, *MNRAS*, submitted (Paper VI)
- Bournaud F., Jog C. J., Combes F., 2007, *A&A*, 476, 1179
- Bournaud F., Elmegreen B. G., Teyssier R., Block D. L., Puerari I., 2010, *MNRAS*, 409, 1088
- Bower R. G. et al., 2004, *MNRAS*, 351, 63
- Bower R. G., Benson A. J., Malbon R., Helly J. C., Frenk C. S., Baugh C. M., Cole S., Lacey C. G., 2006, *MNRAS*, 370, 645
- Cappellari M., Copin Y., 2003, *MNRAS*, 342, 345
- Cappellari M., Emsellem E., 2004, *PASP*, 116, 138
- Cappellari M. et al., 2006, *MNRAS*, 366, 1126
- Cappellari M. et al., 2007, *MNRAS*, 379, 418
- Cappellari M. et al., 2010, *Highlights Astron.*, 15, 81
- Cappellari M. et al., 2011, *MNRAS*, submitted (Paper VII)
- Cattaneo A., Dekel A., Devriendt J., Guiderdoni B., Blaizot J., 2006, *MNRAS*, 370, 1651
- Chen C., Côté P., West A. A., Peng E. W., Ferrarese L., 2010, *ApJS*, 191, 1
- Cimatti A. et al., 2008, *A&A*, 482, 21
- Cole S. et al., 2001, *MNRAS*, 326, 255
- Conselice C. J., 2006, *MNRAS*, 373, 1389
- Courteau S., Dutton A. A., van den Bosch F. C., MacArthur L. A., Dekel A., McIntosh D. H., Dale D. A., 2007, *ApJ*, 671, 203
- Cox T. J., Dutta S. N., Di Matteo T., Hernquist L., Hopkins P. F., Robertson B., Springel V., 2006, *ApJ*, 650, 791
- Crook J. R. et al., 2007, *ApJ*, 655, 790
- Croton D. J. et al., 2006, *MNRAS*, 365, 11
- Daddi E. et al., 2005, *ApJ*, 626, 680
- Davies R. L., Efstathiou G., Fall S. M., Illingworth G., Schechter P. L., 1983, *ApJ*, 266, 41
- Davies R. L., Sadler E. M., Peletier R. F., 1993, *MNRAS*, 262, 650
- Davis T. A. et al., 2011, *MNRAS*, in press (Paper V)
- Dekel A., Birnboim Y., 2006, *MNRAS*, 368, 2
- de Vaucouleurs G., 1959, *Handb. Phys.*, 53, 311
- de Vaucouleurs G., 1963, *ApJS*, 8, 31
- de Vaucouleurs G., de Vaucouleurs A., Corwin J. R., 1976, *Second Reference Catalogue of Bright Galaxies*. Univ. Texas Press, Austin
- de Vaucouleurs G., de Vaucouleurs A., Corwin H. G., Jr, Buta R. J., Paturel G., Fouque P., 1991, *Third Reference Catalogue of Bright Galaxies*, Vols 1–3. Springer-Verlag, Berlin
- de Zeeuw P. T. et al., 2002, *MNRAS*, 329, 513
- Di Matteo T., Springel V., Hernquist L., 2005, *Nat*, 433, 604
- Djorgovski S., Davis M., 1987, *ApJ*, 313, 59
- Dressler A., Lynden Bell D., Burstein D., Davies R. L., Faber S. M., Terlevich R., Wegner G., 1987, *ApJ*, 313, 42
- Dumas G., Mundell C. G., Emsellem E., Nagar N. M., 2007, *MNRAS*, 379, 1249
- Dunkley J. et al., 2009, *ApJS*, 180, 306
- Efron B., Tibshirani R., 1993, *An Introduction to the Bootstrap*. Chapman & Hall, New York
- Emsellem E. et al., 2004, *MNRAS*, 352, 721
- Emsellem E. et al., 2007, *MNRAS*, 379, 401
- Emsellem E. et al., 2011, *MNRAS*, submitted (Paper III)
- Faber S. M., Jackson R. E., 1976, *ApJ*, 204, 668
- Faber S. M. et al., 1997, *AJ*, 114, 1771
- Faber S. M. et al., 2007, *ApJ*, 665, 265
- Falcón-Barroso J. et al., 2006, *MNRAS*, 369, 529
- Ferrarese L., van den Bosch F. C., Ford H. C., Jaffe W., O’Connell R. W., 1994, *AJ*, 108, 1598
- Ferrarese L. et al., 2006, *ApJ*, 644, L21
- Gerhard O. E., 1993, *MNRAS*, 265, 213
- Giovanelli R. et al., 2005, *AJ*, 130, 2598
- Graham A. W., 2004, *ApJ*, 613, L33
- Graham A. W., Worley C. C., 2008, *MNRAS*, 388, 1708
- Granato G. L., De Zotti G., Silva L., Bressan A., Danese L., 2004, *ApJ*, 600, 580
- Hernquist L., 1992, *ApJ*, 400, 460
- Hopkins P. F., Hernquist L., Cox T. J., Keres D., Wuyts S., 2009, *ApJ*, 691, 1424
- Hubble E. P., 1936, *Realm of the Nebulae*. Yale Univ. Press, New Haven
- Huchra J., Davis M., Latham D., Tonry J., 1983, *ApJS*, 52, 89
- Huchra J. P., Geller M. J., Clemens C. M., Tokarz S. P., Michel A., 1992, *Bull. d’Inf. Cent. Donnees Stellaires*, 41, 31
- Huchra J. P. et al., 2005, in Colless M., Staveley-Smith L., Stathakis R., eds, *Proc. IAU Symp. 216, Maps of the Cosmos*. Astron. Soc. Pac., San Francisco, p. 170
- Illingworth G., 1977, *ApJ*, 218, L43
- Jarrett T. H., Chester T., Cutri R., Schneider S., Skrutskie M., Huchra J. P., 2000, *AJ*, 119, 2498
- Jeans J. H., 1922, *MNRAS*, 82, 122
- Jeong H. et al., 2009, *MNRAS*, 398, 2028
- Jesseit R., Naab T., Peletier R. F., Burkert A., 2007, *MNRAS*, 376, 997
- Jesseit R., Cappellari M., Naab T., Emsellem E., Burkert A., 2009, *MNRAS*, 397, 1202
- Johansson P. H., Naab T., Ostriker J. P., 2009, *ApJ*, 697, L38
- Józsa G. I. G., Oosterloo T. A., Morganti R., Klein U., Erben T., 2009, *A&A*, 494, 489
- Karachentsev I. D., Nasonova O. G., 2010, *MNRAS*, 405, 1075
- Kereš D., Katz N., Weinberg D. H., Davé R., 2005, *MNRAS*, 363, 2
- Khochfar S., Burkert A., 2003, *ApJ*, 597, L117
- Khochfar S., Burkert A., 2005, *MNRAS*, 359, 1379
- Khochfar S., Ostriker J. P., 2008, *ApJ*, 680, 54
- Khochfar S., Silk J., 2006, *ApJ*, 648, L21
- Khochfar S., Silk J., 2009, *MNRAS*, 397, 506
- Khochfar S. et al., 2011, *MNRAS*, submitted (Paper VIII)
- Kochanek C. S. et al., 2001, *ApJ*, 560, 566
- Kormendy J., Bender R., 1996, *ApJ*, 464, L119
- Kormendy J., Richstone D., 1995, *ARA&A*, 33, 581
- Kormendy J., Fisher D. B., Cornell M. E., Bender R., 2009, *ApJS*, 182, 216
- Krajnović D., Cappellari M., de Zeeuw P. T., Copin Y., 2006, *MNRAS*, 366, 787
- Krajnović D. et al., 2008, *MNRAS*, 390, 93
- Krajnović D. et al., 2011, *MNRAS*, submitted (Paper II)
- Kuntschner H. et al., 2006, *MNRAS*, 369, 497
- Kuntschner H. et al., 2010, *MNRAS*, 408, 97
- Landsman W. B., 1993, in Hanisch R. J., Brissenden R. J. V., Barnes J., eds, *ASP Conf. Ser. Vol. 52, Astronomical Data Analysis Software and Systems II*. Astron. Soc. Pac., San Francisco, p. 246
- Lauer T. R. et al., 1995, *AJ*, 110, 2622
- Lupton R., Blanton M. R., Fekete G., Hogg D. W., O’Mullane W., Szalay A., Wherry N., 2004, *PASP*, 116, 133
- McDermid R. M. et al., 2006, *MNRAS*, 373, 906
- Maraston C., 2005, *MNRAS*, 362, 799
- Markwardt C. B., 2009, in Bohlender D. A., Durand D., Dowler P., eds, *ASP Conf. Ser. Vol. 411, Astronomical Data Analysis Software and Systems XVIII*. Astron. Soc. Pac., San Francisco, p. 251
- Mei S. et al., 2007, *ApJ*, 655, 144
- Morganti R. et al., 2006, *MNRAS*, 371, 157
- Mould J. R. et al., 2000, *ApJ*, 529, 786
- Naab T., Burkert A., 2003, *ApJ*, 597, 893
- Naab T., Burkert A., Hernquist L., 1999, *ApJ*, 523, L133
- Naab T., Jesseit R., Burkert A., 2006a, *MNRAS*, 372, 839
- Naab T., Khochfar S., Burkert A., 2006b, *ApJ*, 636, L81
- Naab T., Johansson P. H., Ostriker J. P., Efstathiou G., 2007, *ApJ*, 658, 710

- Naab T., Johansson P. H., Ostriker J. P., 2009, *ApJ*, 699, L178
- Oosterloo T. et al., 2010, *MNRAS*, 409, 500
- Oser L., Ostriker J. P., Naab T., Johansson P. H., Burkert A., 2010, *ApJ*, 725, 2312
- Paturel G., Petit C., Prugniel P., Theureau G., Rousseau J., Brouty M., Dubois P., Cambr esy L., 2003, *A&A*, 412, 45
- Perlmutter S. et al., 1999, *ApJ*, 517, 565
- Press W. H., Teukolsky S. A., Vetterling W. T., Flannery B. P., 1992, *Numerical Recipes in FORTRAN. The Art of Scientific Computing*, 2nd edn. Cambridge Univ. Press, Cambridge
- Riess A. G. et al., 1998, *AJ*, 116, 1009
- Robertson B., Bullock J. S., Cox T. J., Di Matteo T., Hernquist L., Springel V., Yoshida N., 2006, *ApJ*, 645, 986
- S anchez-Bl azquez P. et al., 2006, *MNRAS*, 371, 703
- Sandage A., 1961, *The Hubble Atlas*. Carnegie Inst., Washington
- Sandage A., 1975, in Sandage A., Sandage M., Kristian J., eds, *Galaxies and the Universe*. Univ. Chicago Press, Chicago, p. 1
- Sarzi M. et al., 2006, *MNRAS*, 366, 1151
- Sarzi M. et al., 2010, *MNRAS*, 402, 2187
- Schechter P., 1976, *ApJ*, 203, 297
- Schlegel D. J., Finkbeiner D. P., Davis M., 1998, *ApJ*, 500, 525
- Scott N. et al., 2009, *MNRAS*, 398, 1835
- Sersic J. L., 1968, *Atlas de Galaxias Australes*. Obser. Astron., C ordoba, Argentina
- Shankar F., Bernardi M., 2009, *MNRAS*, 396, L76
- Shapiro K. L. et al., 2010, *MNRAS*, 402, 2140
- Shen S., Mo H. J., White S. D. M., Blanton M. R., Kauffmann G., Voges W., Brinkmann J., Csabai I., 2003, *MNRAS*, 343, 978
- Skrutskie M. F. et al., 2006, *AJ*, 131, 1163
- Spergel D. N. et al., 2007, *ApJS*, 170, 377
- Springel V., Di Matteo T., Hernquist L., 2005a, *ApJ*, 620, L79
- Springel V. et al., 2005b, *Nat*, 435, 629
- Strateva I. et al., 2001, *AJ*, 122, 1861
- Stumpff P., 1980, *A&AS*, 41, 1
- Taylor E. N., Franx M., Glazebrook K., Brinchmann J., van der Wel A., van Dokkum P. G., 2010, *ApJ*, 720, 723
- Teyssier R., 2002, *A&A*, 385, 337
- Tonry J. L., Dressler A., Blakeslee J. P., Ajhar E. A., Fletcher A. B., Luppino G. A., Metzger M. R., Moore C. B., 2001, *ApJ*, 546, 681
- Trujillo I. et al., 2006, *MNRAS*, 373, L36
- Trujillo I., Cenarro A. J., de Lorenzo-C aceres A., Vazdekis A., de la Rosa I. G., Cava A., 2009, *ApJ*, 692, L118
- Tully R. B., Fisher J. R., 1977, *A&A*, 54, 661
- Tully R. B., Shaya E. J., Karachentsev I. D., Courtois H. M., Kocevski D. D., Rizzi L., Peel A., 2008, *ApJ*, 676, 184
- Tully R. B., Rizzi L., Shaya E. J., Courtois H. M., Makarov D. I., Jacobs B. A., 2009, *AJ*, 138, 323
- Valentijn E. A. et al., 2007, in Shaw R. A., Hill F., Bell D. J., eds, *ASP Conf. Ser. Vol. 376, Astronomical Data Analysis Software and Systems XVI*. Astron. Soc. Pac., San Francisco, p. 491
- Valentinuzzi T. et al., 2010, *ApJ*, 712, 226
- van den Bergh S., 2007, *AJ*, 134, 1508
- van der Marel R. P., Franx M., 1993, *ApJ*, 407, 525
- van der Wel A., Bell E. F., van den Bosch F. C., Gallazzi A., Rix H.-W., 2009, *ApJ*, 698, 1232
- van Dokkum P. G. et al., 2008, *ApJ*, 677, L5
- Weijmans A. et al., 2009, *MNRAS*, 398, 561
- Weijmans A., Bower R. G., Geach J. E., Swinbank A. M., Wilman R. J., de Zeeuw P. T., Morris S. L., 2010, *MNRAS*, 402, 2245
- York D. G. et al., 2000, *AJ*, 120, 1579
- Young L. M. et al., 2011, *MNRAS*, submitted (Paper IV)

## SUPPORTING INFORMATION

Additional Supporting Information may be found in the online version of this article:

**Table 3.** The ATLAS<sup>3D</sup> sample of 260 early-type (E and S0) galaxies.

**Table 4.** The 611 spiral galaxies in the ATLAS<sup>3D</sup> parent sample.

Please note: Wiley-Blackwell are not responsible for the content or functionality of any supporting materials supplied by the authors. Any queries (other than missing material) should be directed to the corresponding author for the article.